Author/s:
Roy, A;Chow, SH;Randolph, MF;O'loughlin, CD

Title:
Consolidation effects on uplift capacity of shallow horizontal plate anchors in dilating sand

Date:
2022-11-01

Citation:
Roy, A., Chow, S. H., Randolph, M. F. & O'loughlin, C. D. (2022). Consolidation effects on uplift capacity of shallow horizontal plate anchors in dilating sand. Geotechnique, 72 (11), pp.957-973. https://doi.org/10.1680/jgeot.20.P.117.

Persistent Link:
https://hdl.handle.net/11343/279372

Consolidation effects on uplift capacity of shallow horizontal plate anchors in dilating sand

A. Roy[1], S.H Chow[2], M.F. Randolph[3], C.D. O'Loughlin[4]

1, 3, 4 Centre for Offshore Foundation Systems, University of Western Australia, Australia

[2] Department of Infrastructure Engineering, the University of Melbourne, Australia

Article manuscript submitted to Geotechnique

First submission: April,2020

[1]Corresponding Author
PhD student, Centre for Offshore Foundation Systems (BEng, MEng)
The University of Western Australia
35 Stirling Highway, Crawley WA 6009, Perth, Australia
E-mail: anamitra.roy@research.uwa.edu.au
Orcid: (0000-0002-3093-1848)

[2]Senior Lecturer, Department of Infrastructure Engineering (BEng, MEng, PhD)
Engineering Block B, Grattan Street, Parkville
The University of Melbourne, Victoria 3010, Australia
Phone: +61 3 9035 7504
E-mail: shiaohuey.chow@unimelb.edu.au
Orcid: (0000-0002-5442-0014)
Formerly at the University of Western Australia

[3]Professor, Centre for Offshore Foundation Systems (MA, PhD, FAA, FREng, FRS, FTSE, FIEAust, CPEng)
The University of Western Australia
35 Stirling Highway, Crawley WA 6009, Perth, Australia
Phone: +61 8 6488 3075, Fax: +61 8 6488 1044
E-mail: mark.randolph@uwa.edu.au

[4]Associate Professor, Centre for Offshore Foundation Systems (BEng, PhD)
The University of Western Australia
35 Stirling Highway, Crawley WA 6009, Perth, Australia
Phone: +61 8 6488 6488, Fax: +61 8 6488 1044
E-mail: conleth.oloughlin@uwa.edu.au
Orcid: (0000-0002-5823-6265)

Number of words	6477 (excluding abstract, appendix, references and captions)
Number of figures	14
Number of tables	04

Consolidation effects on uplift capacity of shallow horizontal plate anchors in dilating sand

A. Roy[1], S.H Chow[2], M.F. Randolph[3], C.D. O'Loughlin[4]

[1, 3, 4] Centre for Offshore Foundation Systems, University of Western Australia, Australia

[2] Department of Infrastructure Engineering, the University of Melbourne, Australia

Abstract

This paper examines the effect of consolidation on a shallowly embedded horizontal plate anchor in medium dense and dense sand using centrifuge tests, where the loading rate was varied over four orders of magnitude. The experimental results show a 4.8 to 5.5 times increase in anchor capacity as the consolidation condition changes from drained to undrained, driven by a steadily increasing negative excess pore pressure with increasing loading rate. At the highest loading rate, under undrained conditions, the measured maximum negative excess pore pressures reaches a steady limit suggesting the occurrence of cavitation. This increase in anchor capacity with non-dimensional displacement rate is captured using a 'backbone curve' interpretation framework that describes the change in capacity between the limiting values of drained and undrained anchor capacity. Calculation of drained anchor capacity is straightforward relative to the more challenging problem of calculating undrained capacity, particularly during cavitation. This was addressed separately through a numerical parametric study (pure undrained analysis) using a bounding surface soil model involving different water depths (cavitation potential), densities and embedment ratios. The numerical results are then systematised into a simple extended analytical solution to allow estimation of undrained anchor capacity under different densities and water depths.

Keywords

Plate anchors; consolidation; cavitation; bounding surface model; sand

List of notations

δ	Anchor displacement
δ_{soil}	Soil displacement
σ_{vo}	Total overburden stress
σ'_v	Vertical effective stress

σ'_n	Normal effective stress
μ	Kinematic viscosity
μ_{20}	Kinematic viscosity at 20˚ C
$\Delta\gamma^p_{oct}$	Incremental octahedral plastic shear strain
γ'	Effective unit weight of soil
ϕ	Friction angle
ψ_d	Dilation angle
τ_f	Shear stress
θ	Lode angle
ψ	State parameter
A	Area of the plate anchor
B	Plate width (strip or rectangular anchor)
c_v	Consolidation coefficient
d	Dimension
d_{50}	Median particle size
e	Void ratio
$F_{u\_ps,dr}$	Uplift factor in plane strain under drained conditions
g	Centrifuge acceleration level
H	Embedment depth of the anchor plate
I_R	Relative dilatancy index
α, β, j	Fitting constants
K_0	Coefficient of earth pressure
K_w	Bulk modulus of water
L	Plate length (rectangular anchor)
N_γ	Anchor factor
$N_{\gamma,dr}$	Drained anchor factor
$N_{\gamma,un}$	Undrained anchor factor
P_a	Atmospheric pressure
p'	Mean effective stress
q_{net}	Net cone resistance
q	Mobilised anchor capacity
q_u	Peak anchor capacity, resistance
$q_{u,dr}$	Peak anchor capacity (drained conditions)
$q_{u,un}$	Peak anchor capacity (undrained conditions)
$q_{u,ref}$	Resistance at a reference velocity
R_D	Relative density
S_f	Shape factor
T	Temperature
t	Thickness of plate anchor

V	Dimensionless velocity
V_{dr}	Drained limit for dimensionless velocity
V_{un}	Undrained limit for dimensionless velocity
V_{50}	Dimensionless velocity at 50% degree of consolidation
u_{cav}	Cavitation pressure of water (negative value)
u_{hydro}	Initial hydrostatic pore pressure at soil surface
Δu_{max}	Maximum magnitude of pore pressure change limited by cavitation
Δu_{cav}	maximum change of pore pressure possible at a location prior to cavitation
u	Pore pressure
u_2	Measured pore pressure at cone shoulder
v	Velocity
z	Depth

Introduction

Increasing motivation to extract energy from offshore renewable sources has seen the development of a number of floating renewable energy devices for harnessing wind and wave power (Hallowell et al. 2018, Al Shami et al. 2019). Such devices are subjected to high uplift and/or lateral loads under wind and wave action, such that a safe and reliable anchoring system for keeping these devices on station is a critical component of the overall infrastructure. An efficient mooring solution for these applications could be provided by plate anchors due to their high efficiency in resisting uplift loading (Bradshaw et al. 2015, O'Loughlin et al. 2018, Al Hakeem & Aubeny 2019). To explore the mooring potential of plate anchors for offshore renewable energy applications, recent studies on plate anchors have focused on investigating their performance in sands, which are typical of seabed conditions where floating renewable energy devices might be located (e.g. Knappett et al. 2015, Giampa et al. 2017, Chow et al. 2018).

Installation (and anchoring) of floating energy devices are relevant for relatively deep sea, where they can take advantage of superior wind speeds and high wave energy (e.g. the Hywind floating wind farm moored in 95 to 129 m water depths off the coast of Scotland). Under such aggressive conditions, the anchors will be subjected to rapid loading, leading to changing consolidation conditions or 'rate effects' in soil resistance and hence in anchor capacity. Rate effects on soil resistance comprise two components: (a) consolidation effects due to generation of excess pore pressure, and (b) viscous (rheological) effects (Lehane et al. 2009). For the problem considered here (in sand), the contribution of viscous effects is negligible relative to consolidation effects (e.g. Dayal & Allen 1975, Watanabe & Kusakabe 2013), such that in the current context 'rate effects' are considered analogous to 'consolidation effects'. The significance of consolidation effects during rapid shearing in sand was recognised as early as the 1970s in studies of retrieval lift operations of objects embedded in the seafloor (Muga 1968); and later in various other offshore applications, such as ploughing (van Os & van Leussen 1987, Palmer 1999), in-service performance of suction caissons for offshore wind turbines (Achmus & Thieken 2014, Bienen et al. 2018), upheaval buckling of pipelines (Bransby & Ireland 2009, Williams et al. 2013) and installation of drag embedded fluke anchors (Heurlin et al. 2015). In particular, consolidation effects could have severe consequences in dense, dilating sand (as typically found offshore), where dilation induced negative excess pore pressures result in significantly increased soil resistance during ploughing or anchor installation (e.g. Palmer 1999, Heurlin et al. 2015).

Quantification of consolidation effects for boundary valued problems can be achieved using a dimensionless velocity term ($V = vd/c_v$), where v, d and c_v denote velocity or loading rate, drainage path length and the coefficient of consolidation for the soil, respectively (Finnie & Randolph 1994). With increasing V, the normalised soil resistance for a given boundary value problem (i.e. resistance at a given velocity over the reference undrained/drained resistance at a reference velocity $q_u/q_{u,ref}$) varies non-linearly as the consolidation regimes changes from drained to partially drained to undrained, with V_{dr} and V_{un} marking the boundary between drained and undrained regimes respectively (e.g. Finnie & Randolph 1994, Chung et al. 2006, Lee & Randolph 2011). For applications in sand (Fig. 1), this variation in resistance, commonly known as a 'backbone curve', can be quantified using (Chow et al. 2020):

$$\frac{q_u}{q_{u,dr}} = \frac{1+\frac{q_{u,un}}{q_{u,dr}}\left(\frac{V}{V_{50}}\right)^c}{1+\left(\frac{V}{V_{50}}\right)^c} \qquad (1)$$

where $q_{u,un}/q_{u,dr}$ is the ratio of the limiting undrained resistance to the reference drained resistance, V_{50} is the value of V at 50% degree of consolidation and c is a constant controlling the evolution of $q_u/q_{u,dr}$ within the partially drained region. Note that the original expression in Chow et al. (2020) also considered viscous rate effects, which are ignored here as the change in resistance due to viscous effects will be negligible relative to the change due to consolidation effects (as discussed earlier).

Chow et al. (2020) also highlights the challenges in estimating undrained capacity of an anchor in sand analytically, particularly in the scenario where cavitation may occur in a dilating dense sand. Cavitation occurs when vapour bubbles form within the pore water at an absolute magnitude of pore water pressure equal to the vapour pressure of water (i.e. approximately -100 kPa). The potential for cavitation to occur is influenced by the initial hydrostatic pore pressure (u_{hydro}), as evident from triaxial tests (Mcmanus & Davis 1997) and suction bucket tension loading tests (Andersen et al. 1994, Bye et al. 1995, Byrne 2000, Kelly et al. 2003, Bienen et al. 2018). Since cavitation is only triggered at around -100 kPa, the potential for cavitation to occur for a soil in a state of shear (and at a given density) is higher in the water depths relevant for floating renewable energy devices.

This paper investigates consolidation effects for vertical uplift capacity (q_u) of a horizontal plate anchor shallowly embedded in sand through centrifuge modelling and numerical analysis. The centrifuge study involved 26 uplift tests on pre-embedded rectangular plate anchors in both medium dense and dense sand, where the uplift velocity varied over four orders of magnitude. In order to extend the consolidation regime from drained to undrained, the coefficient of consolidation (c_v) was scaled down in the tests by reducing the soil permeability,

achieved by saturating the sand using a viscous pore fluid instead of water, similar to the approach described in Adamidis & Madabhushi (2015). Consolidation effects on plate anchor capacity are then quantified using a backbone curve that spans between the limiting drained and undrained capacities. The limiting undrained anchor capacity ($q_{u,un}$) under cavitation is further quantified through numerical analyses under a range of soil conditions and subsequently synthesised in a simple analytical framework, such that it may be used readily as a calculable input for the backbone curve.

Experimental methodology

Modelling using viscous pore fluid

In order to reduce c_v, a viscous pore fluid known as methocel cellulose ether (Food grade F450) at a concentration of 2.2% was used to saturate the sand samples. The methocel solution was prepared according to the hot/cold mixing technique (Dow 2002). The viscosity of the solution is shearing rate and temperature dependent (Adamidis & Madabhushi 2015). These dependencies were assessed using a series of rotational vane viscometer tests across a temperature (T) range between 17°C and 32°C (Fig. 2) and a range of rotation rates up to 20 s^{-1}, which covers the expected range of shearing rates (v/d = 0.0003 to 3.13 s^{-1}) for the soil in the anchor uplift tests. With no significant change expected in the measured kinematic viscosities (μ) over the relatively low range of shearing rates considered here (Adamidis & Madabhushi 2015), the variation in with temperature was fitted using the exponential expression:

$$\frac{\mu}{\mu_{20°C}} = 2.23e^{-0.04T} \qquad (2)$$

with $\mu_{20°C}$ = 530.3 cSt. Temperature in the centrifuge was continuously monitored during testing, so Eqn. (2) allowed accurate estimation of the pore fluid viscosity for evaluating c_v and V for the anchor tests.

Model plate anchors

Sand blasted stainless steel rectangular plate anchors of width (B) 20 mm, length (L) 40 mm and thickness (t) 6 mm were used in this study (see Fig. 3(b)). The anchor width was selected to ensure that potential grain size effects are negligible, achieved by ensuring that the ratio of the plate width to the mean particle size (B/d_{50}) is greater than 35 (Garnier et al. 2007). Selected plates were instrumented with a pore pressure transducer (PPT) (MS54XX with an absolute pressure range of 700 kPa, with a 1.5 mm thick 35 micron polyethylene filter over the sensing element) on the top face of the plate. The PPTs were placed along the central axis at a distance 0.5B from the centre of the plate. Each PPT was calibrated in a pressure chamber prior to the anchor tests, with essentially

identical calibration factors obtained for both positive and negative pressure ranges. As shown in Fig. 3(b), the plates were attached to a smooth modular rigid rod of diameter 4.7 mm and length 80 mm. The rod extended to above the sand surface, such that it was accessible to an electrical actuator, creating a means of loading the plate anchor (see Fig. 3).

Sample preparation details and centrifuge testing procedure

The anchor uplift tests were conducted in a fine sub-angular silica sand, with properties as summarised in Table 1. The sand samples were prepared in centrifuge sample containers ('strongboxes') at two target densities (R_D) of 70% and 48% by air pluviation using an automated sand rainer. Strongboxes of two different sizes were used, the first measuring 1300 mm (length) × 390 mm (breadth) × 225 mm (height) for the dense sample (R_D = 70%) and the second measuring 650 mm (length) × 390 mm (breadth) × 325 mm (height) for the two medium dense samples (R_D ~ 48%). A 20 mm thick gravel layer overlain by a geotextile was placed at the bottom of the strongboxes to facilitate drainage (Fig. 3(a)). To avoid consideration of potential (and variable) installation effects in the interpretation, the anchors were pre-located in the sample (analogous to the 'wished-in-place' approach in numerical modelling). This was achieved by pausing pluviation when the sand reached the required anchor embedment depth, vacuum levelling the sand surface and careful placement of the anchor. Prior to placing the plate anchors, the plate anchor PPTs were saturated in methocel solution for at least 12 hours. Pluviation was then resumed and the top of the sample vacuum levelled such the anchors were at an embedment depth of approximately 60 mm, giving an approximate plate embedment ratio (H/B) to the top of the plate of 2.7.

The sample was then saturated from the base with the methocel solution using a gravity feed method (see Chow et al. 2020). A free layer of the methocel fluid was maintained over the sample during testing including a 4 mm surface layer of baby oil to prevent evaporation and subsequent viscosity changes of the pore fluid in the samples. The height of this layer of free fluid was ~21 mm and ~35 mm for the dense and medium dense samples respectively, giving a hydrostatic pressure (u_{hydro}) of 10.3 kPa and 17.2 kPa respectively at 50g at the soil surface. To ensure saturation was maintained for the plate anchor PPTs, pluviation and sample saturation was completed as soon as possible (typically within 10 hours) after placing the anchors. In-flight measurements of pore pressure (on the anchor) were hydrostatic before loading the anchor, confirming that saturation of the PPTs was maintained.

The density of each sample (and hence R_D) was calculated from global measurements of the sample mass and volume prior to locating the anchors. The appropriateness of this 'average' relative density over the sample height was examined using the empirical correlations developed for the same sand (Roy et. al 2019) from profiles

of net cone resistance (q_{net}) obtained using a miniature piezocone, 10 mm in diameter (Fig. 4(b)). The piezocone tests were performed at a minimum distance of 110 mm from the rigid boundary walls and at a minimum centre to centre distance of 75 mm from the anchors (when measured along width *B*). The net cone resistance was calculated as $q_{net} = q_c - \sigma_{vo} + (1 - \alpha_{cone})u_2$, where q_c is the measured cone resistance, u_2 is the pore pressure measured at the cone shoulder and α_{cone} is the unequal area ratio calibrated in a pressure chamber as 0.74. A velocity of 0.12 mm/s was maintained for these piezocone tests to ensure a drained response, as confirmed from the corresponding pore pressure measurements. Correlations of R_D with q_{net} (Roy et. al 2019) suggested that R_D at the anchor location was approximately ~48% for samples M1 and M2 (similar to the physical measurements) and ~65% for sample D1 (within 5% of the physical measurements). The profiles in Fig. 4 indicate that:

- the spread of q_{net} across the two medium dense samples (M1 and M2) in Fig. 4 is negligible, suggesting relatively similar R_D values (as shown in Fig. 4(b)) and allowing comparison of tests across these two medium dense samples;

- there was a small increase in q_{net} over the course of the testing at the anchor embedment depth, by up to 7% in the medium dense samples (M1 and M2) and up to 13% in the dense sample (D1); these would correspond to a R_D change of 4.8% and 8.5% in the dense and medium dense samples respectively and are not expected to affect the test results significantly.

Centrifuge test program

The anchor tests were conducted in the 1.8 m radius beam centrifuge located at the University of Western Australia (Randolph et al. 1991) at an acceleration level of 50g. The testing program, as outlined in Table 2, involved 26 uplift tests in three methocel saturated sand samples at anchor embedment ratios (*H*/*B*) in the range 2.5 to 2.9 and uplift velocities (v) varying from 0.01 mm/s to 100 mm/s. The minimum centre to centre distance between the plate anchors was 100 mm, established by assuming a pair of slip planes at a very conservative angle of 35° (measured to the vertical), thus avoiding overlapping of the failure mechanism.

Experimental results

The key experimental results are summarised in Table 2. The mobilised anchor resistance (*q*, which is the measured load minus the submerged weight of the anchor and rod, divided by the plate area) and corresponding pore pressure (*u*) responses for tests at different uplift velocities (*v*) are plotted against normalised displacement (δ/B) for all three sand samples in Fig. 5. The peak resistance is also normalised and reported as anchor factors

($N_\gamma = q_u/\gamma' H$, where γ' is the submerged unit weight) in subsequent discussions. As evident in Table 2, seven repeat tests were conducted, with better agreement observed for those in medium dense sand (Samples M1 and M2 with a maximum variation of 5.6% in peak anchor capacity q_u) than those in dense sand (Sample D1 with maximum variation of 13% in q_u), which is consistent with the range in q_{net} from the cone penetrometer tests.

For the slowest tests conducted, with v = 0.01 mm/s in both samples, a purely drained response is obtained, as the PPT measured hydrostatic pressures. As shown in the inset in Fig. 5(a), there is a rapid increase in q as δ/B increases to 2%, while the drained anchor capacity ($q_{u,dr}$) is subsequently attained within δ/B of 15% in medium dense (R_D = 48%) and 10% in dense sand (R_D = 70%). The drained N_γ values obtained in dense sand are about 18% higher than those for medium dense sand. The N_γ values are compared in Fig. 6 with those obtained from previous experiments using plate anchors with different widths (or $B\gamma'/P_a$, where P_a is atmospheric pressure) in the same sand, but in dry conditions (see Roy et al. (2020b)). $B\gamma'/P_a$ in Fig 6 serves as the stress normalisation term to account for the different initial stress levels for the tests in saturated and dry sand. The drained N_γ for R_D = 70% from the current saturated tests match closely with those in dry sand, whereas for the tests with R_D = 48%, a maximum difference of 10% is observed compared with the tests in dry sand. Also shown in Fig. 6 are the analytically determined N_γ values for both relative densities, obtained using the limit-equilibrium method in Giampa et al. (2019). The analytical solution (considered for $B\gamma'/P_a$ = 0.1 with ϕ, ψ_d as per Chakraborty & Salgado 2010), provides reasonable agreement with the measurements in medium dense sand (R_D ~ 48%) but overestimates the measured data by around 28% for the dense sand (R_D ~70%). This overestimation is considered to be due to progressive failure (as explained in Roy et. al (2020b)), that is more dominant in dense sand states than in loose sand states, and is not accounted for in the analytical solution. As shown later in the paper, better agreement is obtained when the drained anchor capacity is calculated using the limit equilibrium approach proposed in Roy et al. (2020b), which encompasses numerically determined anchor capacity factors using the two surface plasticity model adopted in this paper, and accounts for progressive failure effects.

As v is increased, q_u increases progressively as the responses change from drained to partially drained and then towards fully undrained (supported by the pore pressure responses). The corresponding load-displacement responses show an initial stiff response in q before a more gradual increase to attain peak resistance, as shown in the inset in Fig 5. There is remarkable consistency in the gradients of the measured q responses after the initial stiff increase (see Fig 5). However, the displacement required to mobilise the peak capacity increases with increasing v, and also as the response changes from drained to undrained, with the undrained q_u mobilised at a

displacement that is 3.0 (R_D = 70%, D1) and 4.5 - 5.6 (R_D = 48%, M1 and M2) times higher than in the corresponding drained tests. This may well have implications for offshore design, as the maximum permissible displacement criteria may vary from one type of floating structure to another, such that consideration may need to be given to both the limiting capacity and the displacement required to mobilise this capacity. The corresponding pore pressure responses in both dense and medium dense sample under partially drained and undrained conditions show small increases in u in the initial stages, before strong dilation-induced negative excess pore pressure. The shift from positive to negative u becomes faster with increasing R_D, with the point of peak negative $\Delta u/u_{hydro}$ coinciding with q_u (Δu being the measured excess pore pressure).

The experimental results (Fig. 5c) also show that the resistance in the medium dense sample (R_D = 47%) attains a plateau beyond v = 60 mm/s (i.e. test M2_P100a, M2_P60a, M2_T60a in Table 2), indicating that the undrained anchor capacity ($q_{u,un}$) has been attained. The corresponding pore pressure responses at the top of the plate for these cases also show remarkable consistency, reaching a plateau of u ~ –6 kPa. N_γ values for these tests range between 16.55 and 16.9, indicating that the ratio of undrained to drained anchor capacity ($q_{u,un}/q_{u,dr}$) is around 5.3. For the tests in dense sand (R_D = 70%), a similar plateau in q is observed for the tests at v = 10 mm/s (D1_P10a) and v = 30 mm/s (D1_P30a), with q_u of 450 kPa and corresponding u and N_γ values around -40 kPa and 17.2 respectively (Fig. 5a). The q_u values for D1_P10a and D1_P30a are 4.6 times higher than the measured $q_{u,dr}$ values (i.e. test D1_P0.01a) at R_D = 70%, but only 7% higher than the corresponding q_u values obtained at a uplift velocity, v = 10 mm/s at R_D = 48% (i.e. test M1_P10a, M2_T10a in Table 2).The q_u values for D1_P10a and D1_P30a are 4.6 times higher if compared against the measured $q_{u,dr}$ values (i.e. with test D1_P0.01a) in R_D = 70%, but only 7% higher if compared against the corresponding q_u values obtained from v =10 mm/s for R_D = 48% (i.e. test M1_P10a, M2_T10a in Table 2).

The plateau in u (Fig. 5) suggests the occurrence of cavitation in the undrained anchor tests, as observed in triaxial undrained compression tests (McManus & Davis 1997). However, the cavitation pressure, u_{cav} ~ -40 kPa is higher than the expected theoretical cavitation limit of -100 kPa (-1P_a). This may be attributed to the complex pore pressure field around the PPT on top of the plate, which were 0.5B away from the plate centre (Fig. 3). The stress field is clearly dominated by total normal stress towards the centre of the plate, whereas it is dominated by shearing along the edges. The consequence is compression leading to positive excess pore pressures in the centre (Burns & Mayne 1998, Peuchen et al. 2010), and dilation leading to negative excess pore pressure along the edges. The pore fluid may have still cavitated in the shear bands at the edges of the plate, but the average

u values measured at the PPT locations remain higher than the theoretical cavitation pressure. Observations of viscous pore fluid cavitating at a magnitude higher than the theoretical limit of -100 kPa have also been reported from model tests on gravity platforms on dense sand (Andersen et al. 1994).

It is interesting to note that the fastest test, at v = 100 mm/s (D1_T100a), gave q_u = 507 kPa, which is about 11% higher than those for tests at v = 10 mm/s and 30 mm/s. As pore pressure data were not available for the fastest test, it is difficult to ascertain whether this increase was a consequence of viscous rate effects (Lehane et al. 2009, Randolph & Hope 2004, Chow et al. 2020) or a further drop in u. More experimental data at high v would be required to draw an unambiguous conclusion on the precise limits for $q_{u,un}/q_{u,dr}$ in dense sand.

It is important to remember that, although the initial effective stresses were similar in each sample (ignoring the small changes due to differences in sample density), the initial hydrostatic pressure (u_{hydro}) at the soil surface was lower for the dense sample (D1) than the medium dense sample (M1, M2). This could influence the value of $q_{u,un}$ for shallowly buried plates, as it will affect the maximum negative pore pressure possible during cavitation (Andersen et al. 1994). Therefore, the apparently similar range for $q_{u,un}/q_{u,dr}$ ratios in the two samples (from the data on Fig. 5) between 4.84 and 5.46 could be attributed to different u_{hydro} in the two samples. It is worth noting that u_{hydro} is also a necessary input (in addition to R_D) for calculation of $q_{u,un}$, in order to correctly account for the true dilating potential of the sand.

Backbone curve for pure uplift

Consolidation effects on the plate anchor capacity, presented as q_u against V (vd/c_v), are illustrated in Fig. 7(a). The values of c_v for all samples are listed in Table 2 (from Chow et al. 2019). The drainage path length (d) was taken as the radius of an equivalent circle having the same area as the plate anchor (Chung et al. 2006). Fig. 7(a) shows that the drained and undrained capacities were achieved at V_{dr} = 1 and V_{un} = 1000 respectively for both the medium dense and dense samples. To obtain the backbone curve parameters in Eqn. (1), $q_u/q_{u,dr}$ ratios are plotted against V, which collapses the data from both medium dense and dense sand into a tight band (see Fig. 7(b)). The backbone curve parameters are established (from a regression analysis) as $q_{u,un}/q_{u,dr}$ = 5.46, V_{50} = 32 and c = 0.71.

For the horizontal anchors considered here, the value of $q_{u,un}/q_{u,dr}$ ~ 5.46 is much higher than reported by Chow et al. (2020) for inclined anchors in the same sand ($q_{u,un}/q_{u,dr}$ ~ 2.2). This may be explained by the higher kinematic restraints for the failure mechanism of horizontal anchors, characterised by an inverted

trapezoidal block mechanism (see Fig. A1), compared with bilinear or log-spiral rupture surfaces (Choudhary & Dash 2017, Yue et al. 2020). This is supported by the significantly lower values of V_{dr} = 1 and V_{50} = 32 obtained here, compared with V_{dr} = 16 and V_{50} = 175 for inclined anchors. The rapid rise in mobilised anchor capacity and swift transition into the partially drained response for horizontal anchors suggests that careful consideration of consolidation effects is required in the design of vertically loaded plate anchors, especially for situations where the failure mechanism extends in a quasi-vertical direction to the soil surface.

Estimation of undrained capacity

The backbone curve for plate anchor uplift (Eqn. (1)) can be effectively utilised if the ratio of the peak anchor capacities (i.e. $q_{u,un}/q_{u,dr}$) is known a priori. The drained capacity (i.e. $q_{u,dr}$) can be estimated using limit equilibrium methods (LEM) such as those in Murray & Geddes (1987) or Vermeer & Sutjiadi (1985), with refinements to these methods proposed by White et al. (2008) and Giampa et al. (2017, 2019) to guide the choice of peak friction and dilation angles, and more recently by Roy et al. (2020b) to better account for the influence of progressive failure. However, estimation of an operative undrained capacity ($q_{u,un}$) at shallow embedment levels remains complicated (Chow et al. 2020) as it depends on the dilation potential of the sand (controlled by R_D and p') and cavitation. From this standpoint, this section attempts to improve the estimation of $q_{u,un}$ during cavitation through analytical and finite element (FE) undrained analysis. The FE analysis considers strip anchors for computing efficiency, which can then be extended to other anchor types (e.g. the rectangular anchors in the present centrifuge study) through shape factors.

The relevant analytical expression for computing $N_{\gamma,un}$ in the case of (dense) dilation induced cavitation scenarios, based on a modified limit equilibrium approach under plane strain conditions (White et al. 2008, Hao et al. 2018) (see Appendix for details on governing equations) can be expressed as:

$$N_{\gamma,un} = N_{\gamma,dr} + \alpha \frac{H}{B} \left(\frac{\Delta u_{max}}{\sigma'_v} \right)^{\beta} \qquad (3a)$$

$$\Delta u_{max} = u_{hydro} + \gamma_w H - u_{cav}, \text{ where } u_{cav} \geq -100 \text{ kPa} \qquad (3b)$$

where α is a soil mobilisation coefficient during uplift and is a function depending on R_D, β is a fitting constant, u_{hydro} is the hydrostatic pressure at soil surface (as defined earlier), γ_w is the unit weight of water and $\Delta u_{max}/\sigma'_v$ is a normalised maximum pore pressure change according to the limiting pore pressure before cavitation sets in. Eqn. (3a) and (3b) are valid provided that the absolute magnitude of Δu_{max} remains below the limit at which the

dilation induced, negative excess pore pressure result in critical state (constant volume) conditions. A theoretical estimate of this 'critical state' Δu_{max} can be readily obtained using the concepts provided in Fear & Robertson (1995). With the current CSL parameters for UWA sand and assuming even a modest R_D = 40% at H/B = 3, a back analysis shows that this limit is not exceeded at least for 120 metres of water depth and remains valid for even higher water depths if R_D is higher. The term $\Delta u_{max}/\sigma'_v$, introduced to account specifically for different water depths through u_{hydro} (representing water depth), governs the relative magnitude of $N_{\gamma,un}$ with respect to $N_{\gamma,dr}$. It is important to observe that u_{hydro} would be a low value in shallow waters, such that the term $\Delta u_{max}/\sigma'_v$ (σ'_v being equal to $\gamma'H$, which has almost similar magnitude to $\gamma_w H$) would attain a value close to 1.0 in shallow water and increase progressively for deeper water at a given σ'_v. The operative values of α and β in Eqn. (3) are obtained through undrained FE analysis of strip anchors, as explained in the next section and summarised in Eqn. (31).

Numerical model details

The FE analysis was undertaken in Abaqus (Dassault Systemes, 2012) for strip anchors in sand (plane strain) with an unstructured mesh of linear quadrilateral elements (CPE4) (Fig. 8). The FE results were validated with the experiments involving rectangular anchors by applying appropriate shape factors (S_f). The analysis considered a strip anchor with B = 1 m, varying H/B between 2 and 4, R_D between 30% and 85%, with initial hydrostatic pressure (u_{hydro}) at the soil surface between 0 and 50 kPa. Bottom and lateral boundaries of the domain from the centre of the plate were varied in the range of 10B to 12B and 8B to 10B respectively, depending on H/B. The anchor, with slightly filleted corners, was defined as weightless and fully rigid, with its centre taken as the reference point for the application of displacements. The interface between the plate and the soil was modelled as fully rough. The coefficient of earth pressure K_0 was taken as 0.5. An effective stress analysis was achieved in Abaqus using the equivalent total stress analysis approach as adopted in Yi et al. (2012) and Chang (2018), where the pore water stiffness from the bulk modulus of water (K_w) was superimposed into the incremental effective stress stiffness matrix to compute the resulting Δu changes. The changes in Δu at each of the Gauss points was stored as a state variable during the process.

Initial trials showed that the magnitude of u in shear bands and in the zones below the plate can attain large unrealistic negative values lower than the theoretical cavitation limit of water. Once cavitation sets in, the water should change to vapour, limiting further reduction in pore water pressure and releasing the constraint on constant volume (Gawin & Sanavia 2010, Mcmanus & Davis 1997). Hence, a pore pressure cavitation cut-off was introduced to allow realistic estimates of capacity. This was implemented numerically by tracking u at the Gauss

points through a state variable, and by allowing a smooth transition of K_w from its true value of 2 GPa (for undrained conditions) to 0 (fully drained conditions) through a power law reduction of the form $\langle 1 - \left(\frac{\langle -u \rangle}{<-u_{cav}>}\right)^{30} \rangle$ based on the current value of u, where < > are Macaulay brackets, such that $\langle x \rangle = x$ if $x > 0$ and $\langle x \rangle = 0$ if $x < 0$. Such an expression keeps K_w unaltered for positive pore pressure scenarios ($u > 0$) and prevents further build-up of u once u_{cav} is attained.

Constitutive model details

The soil constitutive model adopted in the FE simulations is the two surface plasticity model proposed by Dafalias & Manzari (2004) or Dafalias et al. (2004) as it embraces typical bounding surface plasticity features with kinematic hardening. The model controls sand behaviour with simultaneous interaction of the yield surface with three other surfaces, namely the critical state, bounding and dilatancy surfaces, thus allowing realistic predictions of stresses and strains over a wide range of densities and p' levels. A unique CSL in e - p' space (Li & Dafalias 2012) is used in the current model. Some minor practical modifications, pertaining to the treatment of fabric anisotropy as explained in Roy et al. (2020a), were introduced through scaling factors (f and f_h, see Eqn. (27) to (29) in Table 3) to adjust the influence of the state parameter (ψ) on the model governing equations. Horizontally isotropic sand was assumed with appropriate inputs for the fabric tensor as per Eq. (24) (and **F** as in Eq. (25)). The complete details, calibration procedure against triaxial and simple shear tests and subsequent FE implementation of the model can be found in Roy et al. (2020a) and a brief summary of the model parameters is provided in Table 3.

Validation results and load deformation plots

The FE analysis is validated in Fig. 9 using the centrifuge tests conducted at H/B = 2.7, R_D = 50% and 70% with the surface values of u_{hydro} being taken as 20 kPa and 10 kPa respectively (as per the experiments). A number of trial simulations indicate that cavitation of the pore fluid below the plate occurs at displacement levels of 0.04B (i.e. the displacement level associated with mobilisation of peak undrained capacity). On this basis, the current simulations allow separation between the plate and the soil underneath the anchor, such that the numerically determined $N_{\gamma,un}$ values reflect a condition where the response at the underside of the plate anchor is drained. Using the full theoretical cavitation pressure (u_{cav}) in the simulations of -100 kPa gave an anchor capacity that was on an average 60% higher than the experimental data. From a design perspective, the value of -50 kPa adopted in the simulations appears reasonable (and conservative) but requires further investigation in future work.

The simulated peak values of $N_{\gamma,un}$ was 11.88 at δ/B = 5% for R_D = 50% (with u_{hydro} = 20 kPa) and $N_{\gamma,un}$ = 11.22 for R_D = 70% at δ/B = 3.6% (with u_{hydro} = 10 kPa) respectively. Similar to the trend observed in the experiments, the corresponding undrained limiting capacity is attained at δ/B levels which are 2.0 (R_D = 70%) to 3.3 (R_D = 50%) times higher than the corresponding drained simulations. However, the magnitude of the mobilised displacements in the experiments are approximately ~10-12 times higher than in the simulations, independent of the drainage response. This is partly due to particle scale effects along the shear bands (Ng and Springman 1994, Palmer et al. 2003), but also because the current model uses a lower operative elastic shear modulus than the true G_{max} of the soil and does not consider degradation of elastic shear modulus with strain level (Salgado et al. 2000). Although better agreement with the measured stiffness can be obtained by adjusting the stiffness parameters, this would worsen the agreement with the anchor capacity as adjusting G_0 also affects the plastic response in the model (Roy et al. 2020a).

To enable comparison with the experimental results, the shape factor (S_f) proposed by Dickin (1988) was used to scale the measured results for the rectangular anchors to those for the strip anchor, according to

$$S_f = 1 - \frac{jB}{3LH}(6B - 7H) \qquad (30a)$$

where j was found by Dickin (1988) to be varying from 0.4 at R_D = 33% to 1.0 at R_D = 76% for anchor uplift tests in Erith sand. As the current experiments involved slightly different relative densities, a more representative S_f can be achieved by linearly interpolating between the limits 0.4 and 1.0 for R_D of 33% and 76% as per Eqn. (30b):

$$j = 0.0132\, R_D(\%) - 0.013 \qquad (30b)$$

For R_D ~50% and ~70% in the current experiments, Eqn. (30b) gives j = 0.65 and 0.91 respectively, and ultimately results in S_f values of 1.52 for medium dense sand and 1.73 in dense sand as per Eqn. (30a). These factors result in equivalent strip anchor $N_{\gamma,un}$ values from the experiments of 11.12 (= 16.9/1.52) and 10.65 (= 18.42/1.73) for the tests at R_D = 50% and 70% respectively; these are 6.8% and 5.35% lower than the FE simulated values. In fact, if an S_f of 1.63 at H/B = 2.7 had been chosen for the rectangular plates as per the studies in Frydman & Shaham (1989) of buried slab/anchors, the resulting capacity estimates for R_D = 50% and 70% (considering an S_f = 1.63) would also have been within margins of 12.6% and 9.4% for the two cases. The improved comparison justifies the use of an operative u_{cav} of -50 kPa for these simulations.

Fig. 10 compares the respective failure mechanisms at peak capacity in R_D = 70% at H/B = 2.7 between the undrained (with cavitation) and drained uplift cases in terms of the normalised soil displacements (δ_{soil}/δ)

contours and normalised octahedral plastic shear strain contours ($\Delta\gamma^p_{oct}/\Delta\gamma^p_{oct,max}$). The displacement contours in Fig. 10(a) shows that the influence zone mobilised at peak capacity for the undrained case is larger than for drained conditions, with the corresponding width of the influence zone at the soil surface for undrained uplift being 20% higher than that for drained uplift. On the other hand, Fig. 10(b), comparing the corresponding normalised octahedral plastic shear strain contours ($\Delta\gamma^p_{oct}/\Delta\gamma^p_{oct,max}$) mobilised at peak capacity in R_D = 70%, shows similar inclination of shear bands of 20° ± 3° and 18° ± 4° for the undrained and drained cases respectively, which is slightly higher than a value of 15.6° that would have been obtained using Bolton's (1986) correlations at respective in-situ stress levels. The minor differences in the inclination of the shear bands justifies the use of the same dilation angle in the analytical expression for the drained and undrained cases (as elaborated in the Appendix).

Fig. 11 demonstrates the proximity of the pore fluid to cavitation at peak N_γ for H/B = 2.7 in R_D = 70% with u_{hydro} of 10 kPa. The figure plots the excess pore pressure (Δu) normalised with respect to the maximum (absolute) change possible at that location prior to cavitation (Δu_{cav}). Distinct bands of cavitating pore fluid zones (values close to -1.0) develop along the edges of the plate, mostly coinciding with the shear bands discussed above. There is also a zone of positive excess pore pressure on top of the plate with values higher than 1. This explains why the spot measurements of pore pressure in the experiments were lower than the theoretical value of u_{cav}. Fig 11(b) plots p', q and Δu for two different points located a vertical distance $0.4B$ above the plate: X_1 which is directly above the centre of the plate and X_2 which is located in the zone of intense shearing. With increasing δ/B, the element at X_1 clearly shows evidence of minor dilation, whereas cavitation is evident at X_2 with Δu attaining constancy around -80 kPa (i.e Δu_{cav} at that location). The corresponding p' and q increase sharply during the initial phase of fully undrained loading, but drop in magnitude following the initiation of cavitation, with a switch to a drained (simple shear) loading (i.e. K_w attaining 0).

Numerical results from the parametric study

The above numerical approach has then been extended parametrically to compute $N_{\gamma,un}$ for R_D between 30% and 85%, H/B between 2 and 4 and normalised pore pressure variation potential ($\Delta u_{max}/\sigma'_v$) between 2 and 8.7. For undrained uplift conditions, a change of scale (i.e. changing B but with the same H/B etc.) would result in a proportionate change in the values of $\Delta u_{max}/\sigma'_v$, such that the numerical investigation does not need repeating over different stress levels. Fig. 12(a) plots values of $N_{\gamma,un}$ against different $\Delta u_{max}/\sigma'_v$, showing that $\Delta u_{max}/\sigma'_v$ has a profound influence on $N_{\gamma,un}$. In fact, at values of $\Delta u_{max}/\sigma'_v$ close to 2 (expected in very shallow water as explained earlier), $\Delta u_{max}/\sigma'_v$ seems to be the only influencing factor for $N_{\gamma,un}$ with R_D and H/B having inconsequential effects.

This observation is consistent with the centrifuge test results that suggest similar $N_{\gamma,un}$ numbers for R_D = 50% and 70% at $\Delta u_{max}/\sigma'_v$ levels of around 3.5. This suggests that, if a plate anchor is designed to operate in conditions having periodic variations in water level, extra care needs to be taken in the design.

The results of the FE parametric study can now be used to determine α and β in Eqn. (3). This is achieved by plotting $(N_{\gamma,un} - N_{\gamma,dr})/(H/B)$ (referred to here as the depth normalised capacity difference) against $\Delta u_{max}/\sigma'_v$ as shown in Fig. 12(b). Fig 12b shows that there is a linear relationship between depth normalised capacity difference and $\Delta u_{max}/\sigma'_v$ for different values of relative density, with higher dependence for higher values of R_D reflected in the higher α values, which indirectly influences $N_{\gamma,un}$. $N_{\gamma,un}$). The effect becomes appreciable for $\Delta u_{max}/\sigma'_v$ greater than about 5 (i.e. in deep water relative to the anchor embedment), beyond which the range for $N_{\gamma,un} - N_{\gamma,dr}$ exceeds 20%. The values of peak drained anchor factors (i.e. $N_{\gamma,dr}$) have been obtained using the modified LEM approach based on the same numerical model as described in Roy et al. (2020b), that directly accounts for stress level dependency and progressive failure. The values of α and β for Eqn. (3) were fitted through least square regression to give:

$$\alpha = (0.01 * R_D(\%))^{0.2} \qquad (31a),$$

$$\beta = 1.11 \qquad (31b)$$

Now Eqn. (3), in conjunction with Eqn. (31) and the backbone curve (Eqn. (1)) can be used to predict anchor capacity for different drainage regimes in sand. Further experiments in sands of varying dilative characteristics would assist in quantifying the potential variation of the constants α and β used in Eqn. (3).

The versatility of the backbone curve (Eqn. (1)) and the analytical approach for undrained capacity (Eqn. (30) is evaluated in Fig. 13 by comparing predicted N_γ values against measured values in medium dense (R_D = 50%) and dense (R_D = 70%) sand. Fig. 13 includes the entire set of measured N_γ values from the 26 uplift tests reported in Table 2, reduced to their equivalent strip anchor values by using S_f as described in Dickin (1988) (~1.52 - 1.73) or Frydman & Shaham (1989) (~1.63). For use of Eqn. (1), the predicted $N_{\gamma,dr}$ values have been computed using Eqns. (A1-A4) in the Appendix (further details are provided in Roy et al. (2020b)). $N_{\gamma,un}$ has been obtained from Eqn. (3) using u_{hydro} = 10 kPa and 20 kPa for R_D = 70% and R_D = 50% respectively, and u_{cav} = -50 kPa (as assumed for comparisons with the experiments). Using this approach, the predicted values of $N_{\gamma,un}$ turn out to be 11.55 and 12.5 for R_D = 70% and R_D = 50% respectively, compared to the shape adjusted measured values (i.e. $N_{\gamma,un}/S_f$) which are in the range 10.18 - 11.21 for R_D = 70% and 9.36 - 10.35 and R_D = 50%.

The predicted ratios of $q_{u,un}/q_{u,dr}$ turn out to be 4.34 and 4.84 for R_D = 70% and R_D = 50% respectively, which are about 6% and 13% lower than the (strip converted) experimental values. These ratios of $q_{u,un}/q_{u,dr}$ then allow subsequent prediction of N_γ for any given V through Eqn. (1).

Conclusions

This study has investigated the effect of displacement rate, and hence consolidation, on horizontal plate anchor capacity in medium dense and dense sand through centrifuge experiments covering four orders of magnitude of variation in dimensionless velocity (V = 0.2 to 1930). As V increases in the experiments, the mobilised anchor capacity increases progressively, with pore pressure responses on top of the plate becoming increasingly negative (i.e. suction). At V > 1000, the anchor capacity and pore pressure are observed to reach a plateau, indicating undrained conditions with occurrence of cavitation. However, the measured pore pressures remain higher than the theoretical u_{cav} of -100 kPa, due to the complex pore pressure field at the PPT location. The consolidation effects on anchor capacity can be captured using a backbone curve giving $q_{u,un}/q_{u,dr}$ as a function of V (Eqn. (1)) with fitted parameters of $q_{u,un}/q_{u,dr}$ = 5.46, V_{50} = 32 and c = 0.71.

For application of the backbone curve in practice, estimation of the undrained anchor capacity ($q_{u,un}$) remains the biggest uncertainty due to the pore pressure response, particularly upon cavitation. In order to reduce these uncertainties in estimating $q_{u,un}$, a finite element parametric study was undertaken using a bounding surface plasticity model, taking into account the effects of sand relative density, hydrostatic pressure (controlling cavitation potential) and embedment ratio. The FE study showed that the magnitude of the initial hydrostatic pressure has a profound influence on undrained anchor capacity, meaning that particular care should be exercised when designing plate anchors for use in shallow water.

The influence of the governing factors in undrained plate anchor uplift, as obtained in the parametric study, was represented systematically through a simple analytical model (Eqn. (3)). With proper choice of u_{cav} (influencing the contribution of $\Delta u_{max}/\sigma'_v$), the combined numerical and analytical solution was shown to agree reasonably well with the experimental results. Further work is needed to understand the deviation of u_{cav} from the theoretical value, and to further validate the proposed model on a wider range of sands including natural deposits.

Appendix

This section derives an analytical expression for the undrained capacity ($N_{\gamma,un}$) of a horizontal strip anchor in cavitating sand. The approach follows the limit equilibrium approach for drained capacity ($N_{\gamma,dr}$) assuming an inclined slip model (White et al. 2008, Tom et al. 2017), but with modifications to account for the additional contribution of excess pore pressure. For the inverted trapezoidal mechanism shown in Fig A1, the peak drained uplift resistance force (referred here as P_{dr}) is approximated as the weight of the rigid (trapezoidal) block above the anchor and the shear resistance on the slip planes. Based on Fig A1,

$$P_{dr} = HB\gamma' + \gamma' H^2 \tan(\psi_d) + 2\int_0^H (\tau_f \cos\psi_d - \sigma'_n \sin\psi_d)\frac{dz}{\cos\psi_d} \quad \text{(A1)}$$

Expressing $\tau_f = K_1\sigma'_n$ and $\sigma'_n = K_2\sigma'_v$, Eqn. (A1) becomes

$$P_{dr} = HB\gamma' + \gamma' H^2[\tan(\psi_d) + K_1K_2 - K_2\tan(\psi_d)] \quad \text{(A2)}$$

Finally, $N_{\gamma,dr} = \frac{P_{dr}}{HB\gamma'} = 1 + \frac{H}{B} F_{u\_ps,dr}$ (A3)

where $F_{u\_ps,dr} = [\tan(\psi_d) + K_1K_2 - K_2\tan(\psi_d)]$. A series of drained numerical analyses in Roy et al. (2020b) showed that the drained uplift factor $F_{u\_ps,dr}$ can be represented as:

$$F_{u\_ps,dr} = 0.43 + 0.052I_R \quad \text{(A4)}$$

where $I_R = (= \frac{R_D(\%)}{100}(10 - \ln p') - 1)$ is a relative dilatancy index computed at a mean stress level of $p' = \sigma'_{vo}(0.25\,H/B + 0.5)$.

For undrained conditions, the shear resistance on the slip planes is modified to account for the additional contribution of the excess pore pressures (Δu), resulting in $\sigma'_n = K_2(\sigma'_v - \Delta u)$. Due to cavitation of the pore fluid beneath the plate, potential tensile resistance below the plate is not included, such that the calculated undrained capacity is conservative and also serves to make the analytical model an equivalent of the numerical model reported in the 'Numerical model details' section. Therefore, the peak undrained uplift resistance force (referred to here as P_{un}) may be calculated using a modified form of Eqn. (A2):

$$P_{un} = BH\gamma' + \gamma' H^2[\tan(\psi_d) + K_1K_2 - K_2\tan(\psi_d)] - 2H(\Delta u)(K_1K_2 - K_2\tan(\psi_d)) \quad \text{(A5)}$$

such that the undrained capacity factor ($N_{\gamma,un}$) may be written as:

$$N_{\gamma,un} = \frac{P_{un}}{HB\gamma'} = N_{\gamma,dr} - 2\,\frac{H\,(\Delta u)}{B\sigma'_v}\left(K_1K_2 - K_2\,tan(\psi_d)\right) \quad \text{(A6)}$$

In case of dilation induced cavitation, a term Δu_{max} is introduced (referred to as the pore pressure variation potential), that indicates the maximum negative pore pressure possible at the anchor location before the pore fluid cavitates. Δu_{max} is influenced by the value of the initial hydrostatic pressure (u_{hydro}) at the soil surface and cavitation pressure (u_{cav}). The value of Δu_{max} governs the maximum change in effective stress possible at the anchor location under fully undrained conditions. Therefore,

$$\Delta u_{max} = u_{hydro} + \gamma_w H - u_{cav} \quad \text{(A7)}$$

Eqn. (A6) can then be written as:

$$N_{\gamma,un} = N_{\gamma,dr} + 2\frac{H}{B}\alpha\frac{\Delta u_{max}}{\sigma'_v}(K_1K_2 - K_2\tan(\psi_d)) \quad \text{(A8)}$$

where $\Delta u/\sigma'_v = -\alpha\,\Delta u_{max}/\sigma'_v$ (noting that the minus sign is required as Δu will be negative during dilation) and Δu_{max} is calculated according to Eqn. (A7). The term $\left(K_1K_2 - K_2\,tan(\psi_d)\right)$ in Eqn. (A8) is density and stress level dependent. The additional density dependence can be introduced by introducing a R_D dependence on the term α, whereas the flexibility of additional stress level dependence may be introduced by incorporating a constant β on the stress level term (controlled by $\Delta u_{max}/\sigma'_v$) . α therefore serves as a soil mobilisation coefficient during uplift, whereas β serves as fitting constant. Therefore, Eqn. (A8) can be rewritten in the form:

$$N_{\gamma,un} = N_{\gamma,dr} + \alpha\frac{H}{B}\left(\frac{\Delta u_{max}}{\sigma'_v}\right)^{\beta} \quad \text{(A9)}$$

where $\alpha = f(R_D)$ and β is a fitting constant. Now, as both the analytical model and the FE model encompass the same geotechnical phenomena, the constants α and β can be obtained by best-fitting them over the numerical determined previously $N_{\gamma,un}$ from FE analyses.

Acknowledgements

This work forms part of the activities of the Centre for Offshore Foundation Systems (COFS), currently supported as a node of the Australian Research Council Centre of Excellence for Geotechnical Science and Engineering and as a Centre of Excellence by the Lloyd's Register Foundation. The Lloyd's Register Foundation invests in science, engineering and technology for public benefit, worldwide. The first author would like to acknowledge the financial support provided through an Australian Government Research Training Program

Scholarship. The work is also supported by the Australian Research Council Discovery Grant Scheme DP190100914.

References

Achmus, M. & Thieken, K. (2014). Numerical simulation of the tensile resistance of suction buckets in sand. *Journal of Ocean and Wind Energy* **1** , No. 4, 231–239.

Adamidis, O. & Madabhushi, G.S.P. (2015). Use of viscous pore fluids in dynamic centrifuge modelling. *International Journal of Physical Modelling in Geotechnics* **15** , No. 3, 141–149.

Al Hakeem, N. & Aubeny, C. (2019). Numerical Investigation of Uplift Behavior of Circular Plate Anchors in Uniform Sand. *Journal of Geotechnical and Geoenvironmental Engineering* **145** , No. 9, 04019039.

Al Shami, E., Zhang, R. & Wang, X. (2019). Point absorber wave energy harvesters: A review of recent developments. *Energies* **12** , No. 1, 47

Andersen, K.H., Allard, M.A. & Hermstad, J. (1994). Centrifuge Model Tests of a gravity platform on very dense sand; II : Interpretation. In *7th International Conference on behaviour of Offshore structures*. pp. 255–282.

Bienen, B., Klinkvort, R.T., O'Loughlin, C.D., Zhu, F. & Byrne, B. (2018). Suction caissons in dense sand, part I: Installation, limiting capacity and drainage. *Geotechnique* **68,** No. 11, 937–952.

Bolton, M.D. (1986). The strength and dilatancy of sands. *Géotechnique* **36** , No. 1: 65–78.

Bradshaw, A. S., Giampa, J.R., Dietrich, F., Gilbert, R.B. & Gerkus, H. (2015). Pullout Capacity of Plate Anchors in Sand for Floating Offshore Wind Turbines. In *Proceedings of the 3rd International Symposium on Frontiers in Offshore Geotechnics*. pp. 833–838.

Bransby, M.F. & Ireland, J. (2009). Rate effects during pipeline upheaval buckling in sand. *Proceedings of the ICE - Geotechnical Engineering* **164,** No. 5, 247–256.

Burns, S.E. & Mayne, P.W. (1998). Monotonic and dilatory pore-pressure decay during piezocone tests in clay. *Canadian Geotechnical Journal* **35,** No. 6, 1063–1073.

Bye, A., Erbrich, C., Rognlien, B. & Tjelta, T.I. (1995). Geotechnical design of bucket foundations. *Proceedings of the Annual Offshore Technology Conference*, 1995–May, pp.869–883.

Byrne, B.W. (2000). Investigations of suction caissons in dense sand. PhD thesis, University of Oxford.

Chakraborty, T. & Salgado, R. (2010). Dilatancy and Shear Strength of Sand at Low Confining Pressures. *Journal of Geotechnical and Geoenvironmental Engineering* **136** , No. 1, 527–532.

Chang, K. (2018). Centrifuge modelling and numerical analysis on Dynamically Installed Anchors for floating offshore platforms. PhD thesis, University of Western Australia.

Choudhary, A.K. & Dash, S.K. (2017). Load-Carrying Mechanism of Vertical Plate Anchors in Sand. *International Journal of Geomechanics* **17,** No. 5: 04016116.

Chow, S.H., Roy, A., Herduin, M., Heins,E., King, L., Bienen, B., O' Loughlin, C.D., Gaudin, C. & Cassidy, M.J. (2019). Characterisation of UWA superfine silica sand. *Ocean Graduate School Technical report, The University of Western Australia, GEO 18844*.

Chow, S.H., Diambra, A., O' Loughlin, C.D., Gaudin, C. & Randolph, M.F. (2020). Consolidation effects on monotonic and cyclic capacity of plate anchors in sand. *Geotechnique* **70,** No. 8, 720-731.

Chow, S.H., O' Loughlin, C.D., Gaudin, C & Lieng, J.T. (2018). Drained monotonic and cyclic capacity of a dynamically installed plate anchor in sand. *Ocean Engineering* **148** , 588–601.

Chung, S.F., Randolph, M.F. & Schneider, J.A. (2006). Effect of penetration rate on penetrometer resistance in clay. *Journal of Geotechnical and Geoenvironmental Engineering* **132,** No. 9, 1188–1196.

Dafalias, Y.F. & Manzari, M.T. (2004). Simple Plasticity Sand Model Accounting for Fabric Change Effects. *Journal of Engineering Mechanics* **130,** No. 6, 622–634.

Dafalias, Y.F., Papadimitriou, A.G. & Li, X.S. (2004). Sand plasticity model accounting for inherent fabric anisotropy. *Journal of Engineering Mechanics* **130,** No. 11, 1319–1333.

Dassault Systemes. (2012). *Abaqus analysis users' manual*. Providence, RI, USA: Simula Corp.

Dayal, U. & Allen, J.H. (1975). The Effect of Penetration Rate on the Strength of Remolded Clay and Sand Samples. *Canadian Geotechnical Journal* **12:** 336–348.

Dickin, E.A. (1988). Uplift behavior of horizontal anchor plates in sand. *Journal of geotechnical engineering* **114,** No. 11, 1300–1317.

Dow (2002). Methocel Cellulose Ethers: Technical Handbook. The Dow Chemical Company, Staines, UK.

Fahmy, A.M., de Bruyn, J.R. & Newson, T.A. (2013). Numerical Investigation of the Inclined Pullout Behavior

of Anchors Embedded in Clay. *Geotechnical and Geological Engineering* **31,** No. 5, 1525–1542.

Fear, C.E. & Robertson, P.K. (1995). Estimating the undrained strength of sand: a theoretical framework. *Canadian Geotechnical Journal* **32**, No. 5, 859–870.

Finnie, I.M.S. & Randolph, M.F. (1994). Punch-through and liquefaction induced failure of shallow foundations on calcareous sediments'. In *Proc., 17th Int. Conf. on the Behaviour of Offshore Structures, Boston*. pp. 217–230.

Frydman, S. & Shaham, I. (1989). Pullout capacity of slab anchors in sand. *Canadian Geotechnical Journal* **26,** No. 3, 385–400.

Garnier, J., Gaudin, C., Springman, S.M., Culligan, P.J., Goodings, D., Konig, D., Kutter, B., Philips, R., Randolph, M.F. & Thorel, L. (2007). Catalogue of scaling laws and similitude questions in geotechnical centrifuge modelling. *International Journal of Physical modelling in Geotechnics* **7**, No. 3, 01-23.

Gawin, D. & Sanavia, L. (2010). Simulation of cavitation in water saturated porous media considering effects of dissolved air. *Transport in Porous Media* **81**, No. 1, 141–160.

Giampa, J., Bradshaw, A. & Schneider, J. (2017). Influence of Dilation Angle on Drained Shallow Circular Anchor Uplift Capacity. *International Journal of Geomechanics* **17**, No. 2, 4016056.

Giampa, J.R., Bradshaw, A., Gerkus, H., Gilbert, R.B., Gavin, K.G. & Sivakumar,V. (2019). The effect of shape on the pullout capacity of shallow plate anchors in sand. *Géotechnique* **69** , No. 4, 355–363.

Hallowell, S.T., Arwade, S.R., Fontana, C.M., DeGroot, D.J., Aubeny, C.P., Diaz, B.D., Myers, A.T. & Landon, M.E. (2018). System reliability of floating offshore wind farms with multiline anchors. *Ocean Engineering* **160**, 94–104.

Hao, D., Wang, D., O'Loughlin, C.D. & Gaudin, C. (2018). Tensile monotonic capacity of helical anchors in sand: interaction between helices. *Canadian Geotechnical Journal*, doi:10.1139/cgj-2018-0202.

Heurlin, K. , Resseguier, S., Melin, D. & Nilsen, K.R. (2015). Comparison between FEM analyses and full-scale tests of fluke anchor behavior in silty sand. In *Frontiers in Offshore Geotechnics III - 3rd International Symposium on Frontiers in Offshore Geotechnics, ISFOG 2015*. pp. 875–880.

Kelly, R.B., Byrne, B.W., Houlsby, G.T. & Martin, C.M. (2003). Pressure chamber testing of model caisson foundations in sand. *BGA International Conference on Foundations, Innovations, Observations, Design*

and Practice, (August 2014), pp.421–431.

Knappett, J.A. , Brown, M.J, Aldaikh, H., Patra, S., O'Loughlin, C.D., Chow, S.H., Gaudin, C. & Lieng, J.T. (2015). A review of anchor technology for floating renewable energy devices and key design considerations. *Frontiers in Offshore Geotechnics III*, (October 2016), pp.887–892.

Lee, J. & Randolph, M. (2011). Penetrometer-based assessment of spudcan penetration resistance. *Journal of Geotechnical and Geoenvironmental Engineering* **137**, No. 6, 587–596.

Lehane, B.M. , O'Loughlin, C.D., Gaudin, C. & Randolph, M. (2009). Rate effects on penetrometer resistance in kaolin. *Géotechnique* **59**, No. 1, 41–52.

Li, X.S. & Dafalias, Y.F. (2012). Anisotropic Critical State Theory: Role of Fabric. *Journal of Engineering Mechanics* **138**, No. 3, 263–275.

Li, X.S. & Wang, Y. (1998). Linear Representation of Steady-State Line for Sand. *Journal of Geotechnical and Geoenvironmental Engineering* **124,** No. 12, 1215–1217.

Loukidis, D. & Salgado, R. (2009). Modeling sand response using two-surface plasticity. *Computers and Geotechnics* **36**, No. 1–2, 166–186.

Maitra, S., Chatterjee, S. & Choudhury, D. (2016). Generalized framework to predict undrained uplift capacity of buried offshore pipelines. *Canadian Geotechnical Journal* **53**, No. 11, 1841–1852.

McManus, K.J. & Davis, R.O. (1997). Dilation-induced pore fluid cavitation in sands. *Géotechnique* **47**, No. 1, 173–177.

Muga, B.J. (1968). *Ocean bottom breakout forces, including field test data and the development of an analytical method." Tech. Rep. R591, U.S. Naval Civ. Engrg. Lab., Port Hueneme, California.*

Murray, E.J. & Geddes, J.D. (1989). Resistance of passive inclined anchors in cohesionless medium. *Geotechnique* **39**, No. 3, 417–431.

Murray, E.J. & Geddes, J.D. (1987). Uplift of anchor plates in sand. *ASCE Journal of geotechnical engineering*, **113**, No. 3, 202–215.

Ng, C.W.W. & Springman, S.M. (1994). Uplift resistance of buried pipelines in granular materials. *In Proceedings of the International Conference Centrifuge 94*, Singapore, 753-758. Rotterdam: Balkema

O'Loughlin, C.D., Neubecker, S.R. & Gaudin, C. (2018). Anchoring Systems: Anchor Types, Installation and Design. In *Encyclopaedia of Marine and Offshore Engineering, Wiley*.

Palmer, A. C. (1999). Speed effects in cutting and ploughing. *Géotechnique*, **49**, No. 3, 285–294.

Palmer, A. C., White, D.J., Baumgard, A.J., Bolton, M.D., Barefoot, A.J., Finch, M., Powell, T., Faranski, A.S. & Baldry, J.A.S. (2003). Uplift resistance of buried submarine pipelines: comparison between centrifuge modelling and full-scale tests. *Géotechnique*, **53**, No. 10, 877-883

Peuchen, J., Vanden Berghe, J.F. & Coulais, C. (2010). Estimation of u_1/u_2 conversion factor for piezocone. In *2nd International Symposium on Cone Penetration Testing* (Robertson PK and Mayne PW (eds)). Omnipress, Madison, WI, USA, Paper 1-03.

Randolph, M.F., Jewell, R.J., Stone, K.J.L. & Brown, T.A. (1991). Establishing a new centrifuge facility. In *Proceedings of the International Conference Centrifuge 91,* Boulder, *USA*. pp. 3–9.

Randolph, M.F. & Hope, S. (2004). Effect of cone velocity on cone resistance and excess pore pressures. *Proceedings of the International Symposium on Deformation Characteristics of Geomaterials – IS Osaka*, **10**, No. 1, pp.147–152.

Rokonuzzaman, M. & Sakai, T. (2012). Evaluation of Shape Effects for Rectangular Anchors in Dense Sand: Model Tests and 3D Finite-Element Analysis. *International Journal of Geomechanics* **12**, No. 2, 176–181.

Roy, A., Chow, S.H. , O'Loughlin, C.D., & Randolph, M.F. (2019). Effect of stress history and shallow embedment on centrifuge cone penetration tests in sands, *Proceedings of the 38th International Conference on Offshore Mechanics and Arctic Engineering, Glasgow*

Roy, A., Chow, S.H., O'Loughlin, C.D., Randolph, M.F. & Whyte, S. (2020a). Use of a bounding surface model in predicting element tests and capacity in boundary value problems. *Canadian Geotechnical Journal*, doi.org/10.1139/cgj - 2019 - 0841

Roy, A., Chow, S.H., O'Loughlin, C.D., & Randolph, M.F. (2020b). Towards a simple and reliable method for calculating the capacity of plate anchors in sand. *Canadian Geotechnical Journal*, doi.org/10.1139/cgj - 2020 - 0280

Salgado, R., Bandini, P. & Karim, A. (2000). Shear strength and stiffness of silty sand. *Journal of Geo- technical*

and Geoenvironmental Engineering **126**, No. 5, 451–462.

Sheng, D., Sloan, S.W. & Yu, H.S. (2000). Aspects of finite element implementation of critical state models. *Computational Mechanics* **26,** No. 2, 185–196.

Tom, J.G., O'Loughlin, C.D., White, D.J., Haghighi, A. & Maconochie, A. (2017). The effect of radial fins on the uplift resistance of buried pipelines. *Géotechnique Letters* **7,** No. 1, 60–67.

Van Os, A.G. & van Leussen, W. (1987). Basic research on cutting forces in saturated sand. *Journal of geotechnical engineering*, 113 No. (12), 1501–1516.

Vermeer, P.A. & Sutjiadi, W. (1985). The uplift resistance of shallow embedded anchors. In *Proc., of 11th Int. Conf. of Soil Mechanics and Foundation Engineering, Balkema, Rotterdam, Netherlands*. pp. 1635–1638.

Watanabe, K. and O. Kusakabe (2013). Reappraisal of loading rate effects on sand behaviour in view of seismic design for pile foundation. *Soils and Foundations* **53**, No. 2: 215-231.

White, D.J., Cheuk, C.Y. & Bolton, M.D. (2008). The uplift resistance of pipes and plate anchors buried in sand. *Géotechnique* **58,** No. 10, 771–779.

Williams, E.S., Byrne, B.W. & Blakeborough, A. (2013). Pipe uplift in saturated sand: rate and density effects. *Géotechnique* **63,** No. 11, 946–956.

Yi, J.T., Lee, F.H., Goh, S.H., Zhang, X.Y. & Wu, J.-F. (2012). Eulerian finite element analysis of excess pore pressure response generated by spudcan installation into soft clay. *Computers and Géotechnics* **42,** No. 11, 157-170.

Yue, H., Zhuang, P., Zhang, H. & Song, X. (2020). Failure and deformation mechanism of vertical plate anchors subjected to lateral loading in sand. *International Journal of Geomechanics* **20**, No. 11.

Table captions

Table 1: Physical properties of UWA Silica sand (Chow et al. 2019)

Table 2: Centrifuge testing program

Table 3: Model details

Table 4 : Model parameters for UWA silica sand

Figure captions

Fig. 1 : Backbone curve framework showing the variation in resistance across different consolidation regimes

Fig. 2 : Variation of normalised viscosity with temperature for methocel F450

Fig. 3 : Centrifuge test details: (a) test setup (not to scale), (b) plate anchor model, (c) "wished in place" anchors during sample preparation (d) piezocone testing in saturated sand for sample characterisation

Fig. 4 : Profiles of : (a) net cone tip resistance and (b) relative density estimated using the empirical correlations in Roy et al. (2019)

Fig. 5 : Mobilised capacity and pore pressure response at different uplift velocities in (a) dense sand of R_D = 70% (b) medium dense sand of R_D = 48% (c) medium dense sand of R_D = 47%

Fig. 6 : Comparison of measured N_γ for rectangular plates in dry and saturated drained conditions for (a) dense sand of R_D = 70% - 76% (b) medium dense sand of R_D = 40% - 50%

Fig. 7 : Changing anchor capacity with dimensionless velocity: (a) mobilised anchor capacity (q_u) and (b) normalised mobilised anchor capacity ($q_u/q_{u,dr}$)

Fig. 8: Typical mesh details and boundary conditions for the anchor problem in Abaqus (H/B = 2.7)

Fig. 9: Comparison of simulated and measured anchor factors (adjusted by shape factors) at H/B = 2.7 in: (a) dense sand (R_D = 70%) (b) medium dense sand (R_D = 50%)

Fig. 10: Comparison of numerically determined: (a) failure mechanisms, (b) shear strain distributions at H/B = 2.7 in dense sand (R_D = 70%) for undrained and drained cases

Fig. 11: (a) Contours of excess pore pressure (Δu) normalised by the maximum possible pore pressure change possible prior to cavitation (Δu_{cav}) at H/B = 2.7 in R_D = 70% with u_{hydro} = 10 kPa; (b) variation of p', q and Δu at two different points in the domain

Fig. 12: Variation of: (a) $N\gamma, un$ and (b) depth normalised relative difference, $(N\gamma, un - N\gamma, dr)/(\frac{H}{B})$ from the FE simulations in dense and medium dense sands

Fig. 13: Comparison of measured and predicted anchor factors with changing dimensionless velocity in dense and medium dense sand

Fig. A1: Schematic representation of: (a) plate anchor uplift at failure (b) failure mechanism with inclined slip surface

Table 1: Physical properties of UWA Silica sand (Chow et al. 2019)

Soil properties	UWA Silica sand
Angularity	Sub-rounded to sub-angular
Maximum void ratio(e_{max})[1]	0.789
Minimum void ratio(e_{min})[1]	0.512
Specific gravity[2]	2.67
Uniformity Coefficient (U)	1.73
Particle mean size (d_{50})	0.2 mm

[1] Maximum and minimum void ratios calculated as per AS 1289.5.5.1
[2] Specific gravity of soil particles calculated as per AS 1289.3.5.1

Table 2: Centrifuge testing program

Sample number and R_D	Unit weight, γ' (kN/m^3)	Test ID*	*H/B*	Velocity, *v* (mm/s)	Temperature, *T* (°C)	*V*	Peak mobilised anchor capacity, q_u (kPa)	Peak $N_\gamma = q_u/\gamma' H$
D1 (c_v ~ 4.3 × 10^{-4} m^2/s, R_D = 70%)	10.25	D1_P0.01a	2.6	0.01	-†	0.2	97.27	3.80
		D1_T0.1a	2.8	0.1	19.2	1.9	174.46	6.34
		D1_T0.3a	2.65	0.3	18.7	6.3	211.65	8.28
		D1_P1a	2.55	1	20.6	20.2	215.58	8.59
		D1_T3a	2.7	3	20.4	57.8	365.78	13.82
		D1_T3b	2.5	3	19.2	65.4	317.73	12.92
		D1_P10a#	2.6	10	21.1	194.2	446.97	17.46
		D1_P30a	2.63	30	20.7	585.2	450.98	17.47
		D1_T100a	2.8	100	19.4	1933.7	506.81	18.42
M1 (c_v ~ 7 × 10^{-4} m^2/s, R_D = 48%)	9.87	M1_P0.01a	2.94	0.01	20.7	0.1	93.76	3.36
		M1_T0.01a	2.88	0.01	20.5	0.1	103.25	3.74
		M1_P0.1a	2.93	0.1	20.8	1.2	120.47	4.34
		M1_T1a	2.95	1	21.1	11.5	222.06	7.95
		M1_T3a	2.84	3	20.8	36.0	272.18	10.10
		M1_P10a	2.88	10	20.9	118.2	363.9	13.34
		M1_T100a	2.98	100	21.0	1139.4	467.43	16.55
M2 (c_v ~ 6.4 × 10^{-4} m^2/s, R_D = 47%)	9.86	M2_P0.01a	2.63	0.01	21	0.1	79.1	3.17
		M2_T0.01a	2.66	0.01	21.3	0.1	83.8	3.32
		M2_P0.1a	2.6	0.1	21.2	1.3	113.2	4.59
		M2_P1a	2.6	1	21.3	12.9	169.7	6.89
		M2_T1a	2.8	1	21.3	12.0	193.5	7.3
		M2_P10a	2.6	10	21.3	125.3	317.3	12.88
		M2_T10a	2.67	10	21.3	129.1	343.8	13.56
		M2_P60a	2.7	60	21.3	744.6	432.0	16.9
		M2_T60a	2.61	60	21.34	768.3	404.4	16.31
		M2_P100a	2.65	100	21.2	1270.4	420.6	16.75

* The tests are denoted 'Ax1_Wx2_m', where 'A' is either 'D' or 'M' for a dense or medium dense sample respectively, x1 is the sample number, 'W' is either 'P' or 'T' to denote plates with and without a PPT respectively, x2 is the uplift velocity in mm/s and 'm' denotes the test recurrence ('a' for the first test, 'b' for the second etc.).
† Data not available.
# LVT slip during test

Table 3: Model details

Parameters	Description	Governing equations (Eqn. No)	Notes/Reference
e_o	Controls the intercept of the CSL at very low mean stress levels in e - $(p'/P_a)^{\xi}$ space	$e_c = e_o - \lambda_c \left(p'/P_a\right)^{\xi}$ (4) $\psi = (e - e_c)$ (5)	Li & Wang (1998), Dafalias & Manzari (2004)
λ_c	Controls the slope of the CSL in e - $(p'/P_a)^{\xi}$ space		
ξ	Influences the linearisation of the CSL with p'		
M	Controls the critical state stress ratios in triaxial compression		
c_1	Controls the critical state stress ratios in triaxial extension		
G_0	Elastic shear modulus	$G = G_0 P_a \frac{(2.97-e)^2}{(1+e)} \left(\frac{p'}{P_a}\right)^{1/2}$ (6) $K = G \frac{2(1+\nu)}{3(1-2\nu)}$ (7) $d\varepsilon_e^e = ds/2G$ (8) $d\varepsilon_v^e = dp/K$ (9)	Dafalias & Manzari (2004)
ν	Poisson's ratio		
m	Controls the size of the yield surface	$f = [(\mathbf{r} - \boldsymbol{\alpha}) : (\mathbf{r} - \boldsymbol{\alpha})]^{1/2} - \sqrt{2/3}\, m = 0$ (10)	Dafalias & Manzari (2004)
n_d, n_b	Influences the mobilised stress ratio at peak friction angle and at phase transformation	$\boldsymbol{\alpha}_{\boldsymbol{\theta}}^{\mathbf{a}} = \sqrt{\frac{2}{3}}(M_\theta^a - m)n$ (a = b, d, c) (11) $M_\theta^c = g_1(\theta, c_1)M$ (12) $g_1(\theta, c_1) = \left(\frac{2{c_1}^4}{\left((1+c_1^4) - (1-c_1^4)\cos 3\theta\right)}\right)^{1/4}$ (13) $M_\theta^b = \left[M_\theta^c \exp\left(-n^b\, \psi_f\right)\right]$ (14)* $M_\theta^d = \left[M_\theta^c \exp\left(n^d \psi_f\right)\right]$ (15)*	Dafalias & Manzari (2004), Sheng et al. (2000)

c_h, h_{in}	Plastic modulus constants	$K_p = \frac{2}{3} p' h \left(\boldsymbol{\alpha}_{\boldsymbol{\theta}}^{\mathbf{b}} - \boldsymbol{\alpha} \right) : \mathbf{n}$ (16) $h = \frac{b_o}{(\boldsymbol{\alpha} - \boldsymbol{\alpha}_{\mathbf{in}}) : \mathbf{n}}$ (17) $b_o = h_0 G_0 (1 - c_h e) \left(\frac{p'}{P_a} \right)^{-1/2}$ (18) $h_0 = h_{in} f_h$ (19)*	Dafalias et al. (2004)
A_0	Parameter affecting the rate of dilatancy	$d\varepsilon^p = \langle L \rangle \mathbf{R}$ (20) $\frac{dg}{d\sigma} = \mathbf{R} = \mathbf{R}' + \frac{1}{3} D \mathrm{I} = B\mathbf{n} - C \left(\mathbf{n}^2 - \frac{1}{3} \mathrm{I} \right) + \frac{1}{3} D \mathrm{I}$ (21) $B = 1 + \frac{3(1 - c_2)}{2 c_2} g_2(\theta, c_2) \cos 3\theta,$ $C = 3 \sqrt{\frac{3}{2}} \frac{(1 - c_2)}{c_2} g_2(\theta, c_2)$ $g_2(\theta, c_2) = \frac{2 c_2}{(1 + c_2) - (1 - c_2) \cos 3\theta}$ (22) $D = A_0 \left(\boldsymbol{\alpha}_{\boldsymbol{\theta}}^{\mathbf{d}} - \boldsymbol{\alpha} \right) : \mathbf{n}$ (23)	Dafalias et al.(2004), Loukidis & Salgado (2009)
c_2	Parameter affecting the slope of the plastic potential		
a	Parameter controlling the initial fabric	$F_{11} = F_{22} = 0.5(1 - a), F_{33} = a,$ $F_{ij} = 0 \ \ (when\ i \neq j)$ (24)# $A = g_1(\theta, c_1) \, \mathbf{F} : \mathbf{n},$ (25) $A_c = - \left(\frac{1}{c_1} \right) A_e = \sqrt{\frac{3}{2}} \left(a - \frac{1}{3} \right)$ $A_{ratio} = 2 * \frac{A_e - A}{A_e - A_c}$ (26)	Dafalias et al.(2004)
b_1, b_2, k	Factors to scale the state parameter and plastic modulus for loading conditions other than triaxial compression	$f = \frac{1}{b_1 + b_2 (A_{ratio})^{b_3}}$ (27)* $b_3 = \frac{\log(\frac{1 - b_1}{b_2})}{\log 2}$ $f_h = f^k$ (28)* $\psi_f = f \psi$ (29)*	

* Introduced for state parameter scaling

F_{33} is assumed along the direction parallel to axis of particle deposition

Table 4 : Model parameters for UWA silica sand

Sanisand Model parameters	Symbol	UWA silica sand
Elastic properties	G_0	135
	v	0.14
Critical state properties	e_o	0.812
	λ	0.0189
	ξ	0.7
	M	1.296
	c_1	0.7*
Yield surface	m	0.05
Parameter for Plastic potential gradient	c_2	0.78
Parameters influencing plastic modulus	h_0	7.5
	c_h	1.01
	n_b	2.0
Parameters influencing dilatancy	A_0	0.84
	n_d	3.4
Anisotropy and state parameter scaling parameters	a	0.27
	b_1	2.5
	b_2	-0.833*
	k	1.5

*Assumed

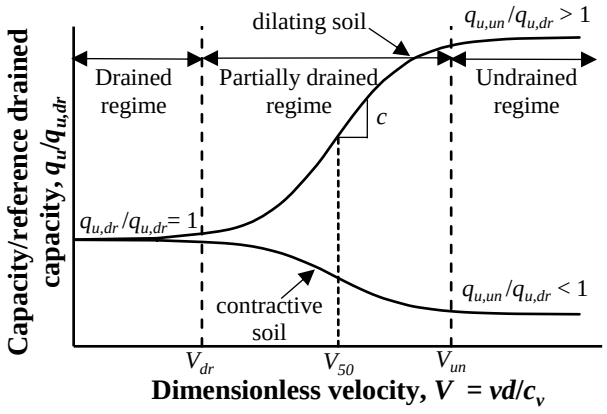

Fig. 1 : Backbone curve framework showing the variation in resistance across different consolidation regimes

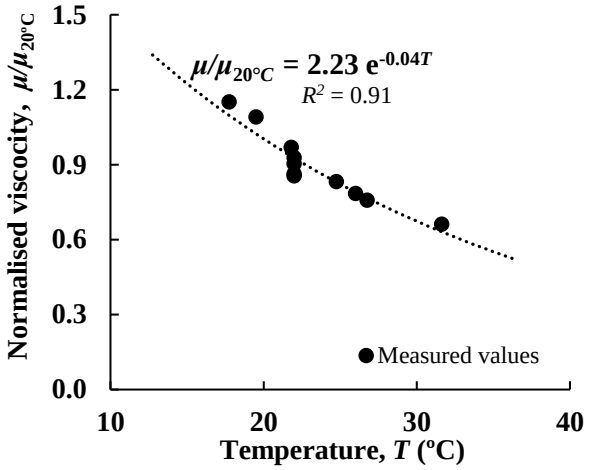

Fig. 2 : Variation of normalised viscosity with temperature for methocel F450

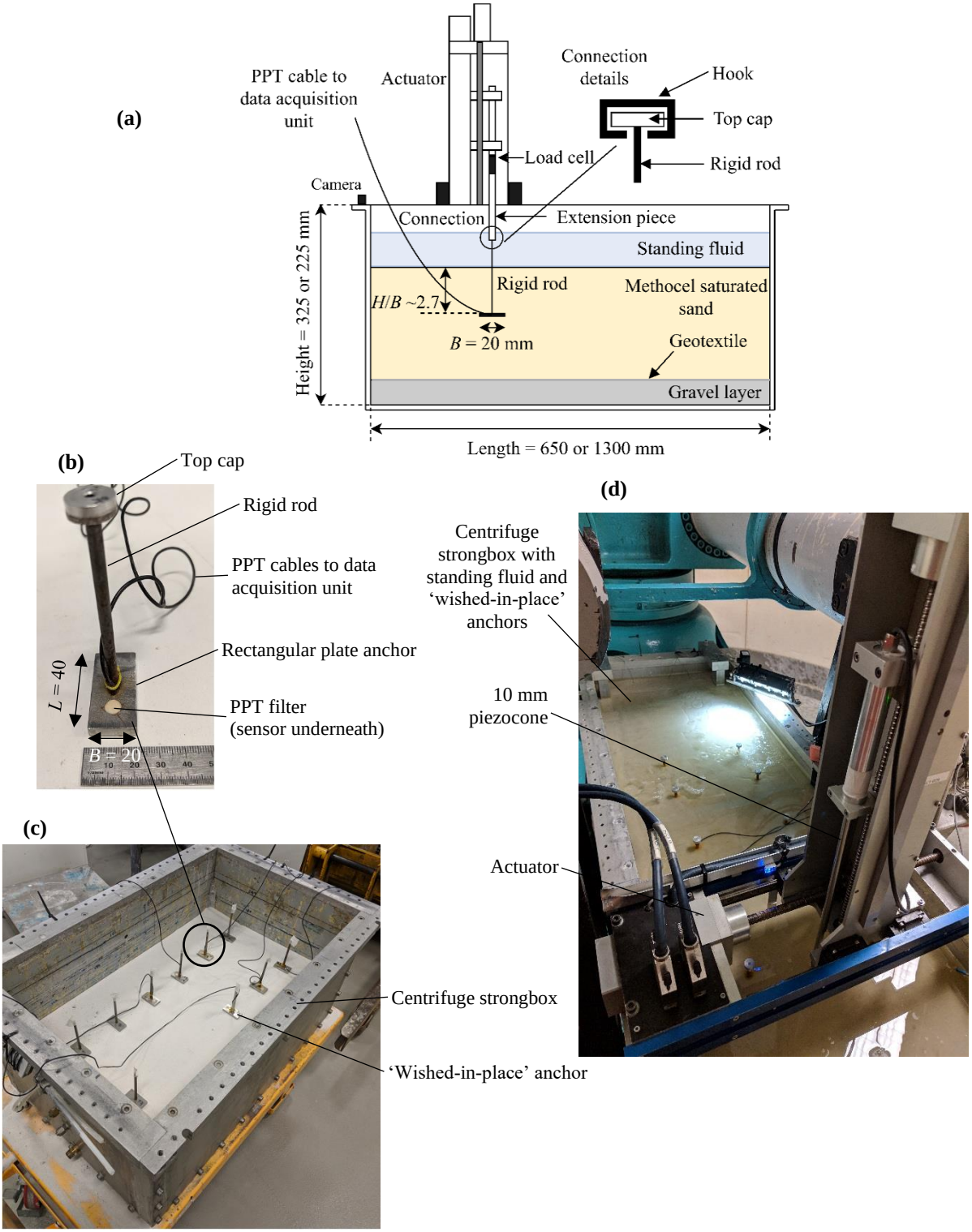

Fig. 3 : Centrifuge test details: (a) test setup (not to scale), (b) plate anchor model, (c) "wished in place" anchors during sample preparation (d) piezocone testing in saturated sand for sample characterisation

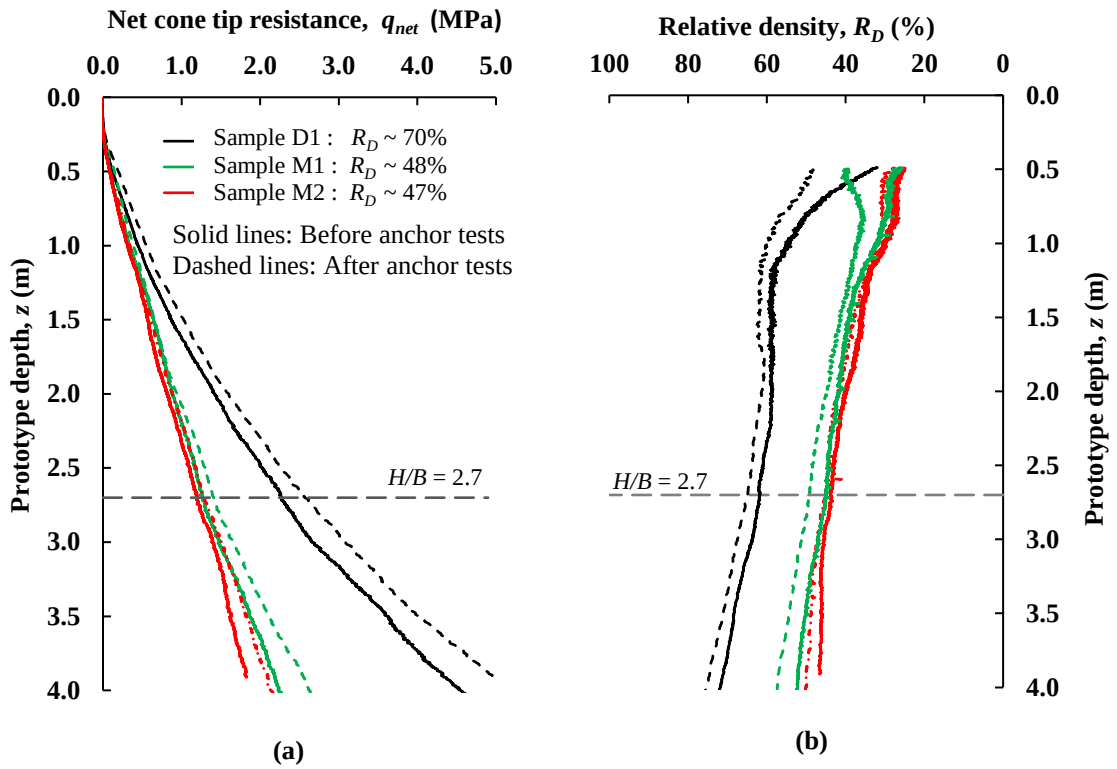

Fig. 4 : Profiles of: (a) net cone tip resistance and (b) relative density estimated using the empirical correlations in Roy et al. (2019)

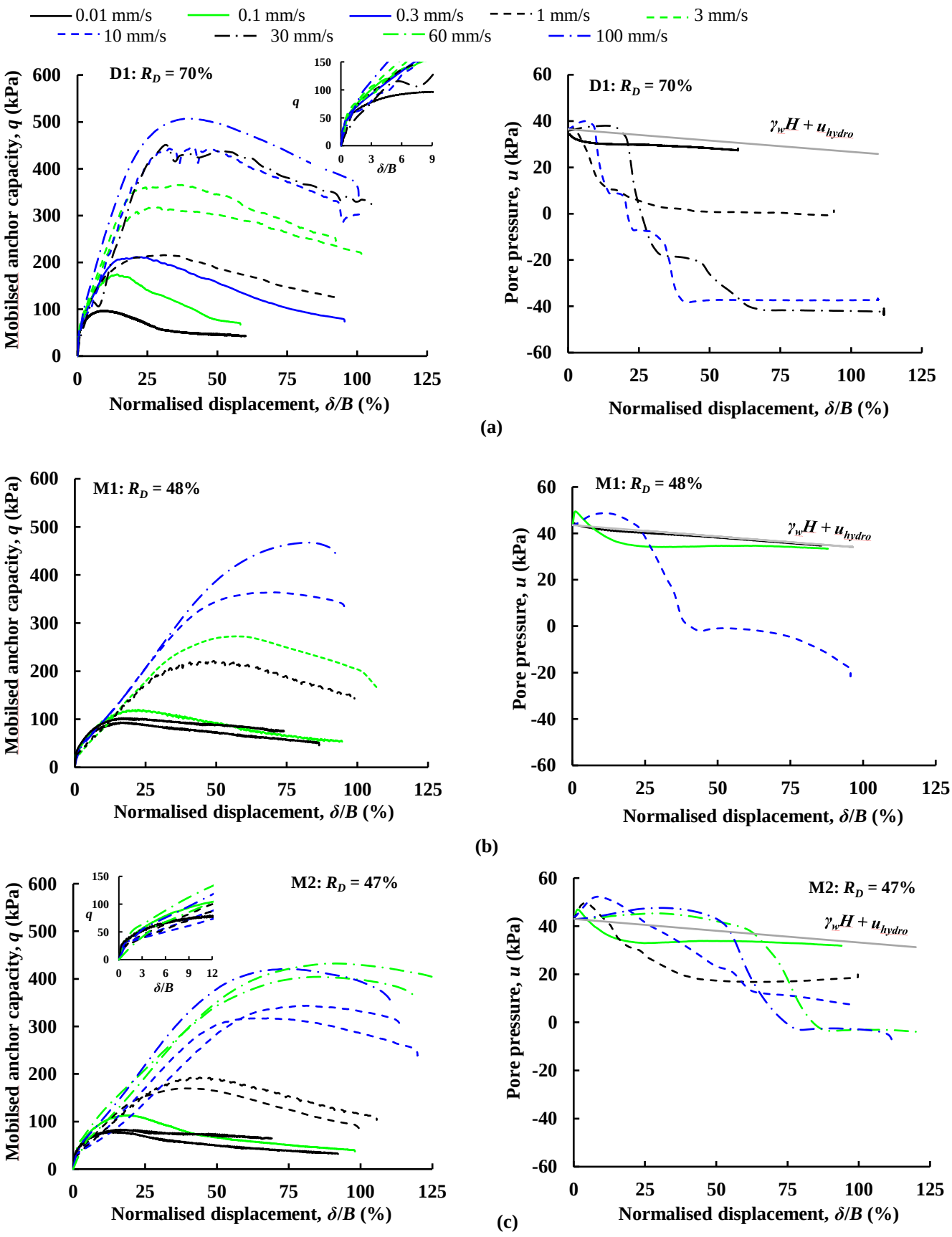

Fig. 5 : Mobilised capacity and pore pressure response at different uplift velocities in (a) dense sand of R_D = 70% (b) medium dense sand of R_D = 48% (c) medium dense sand of R_D = 47%

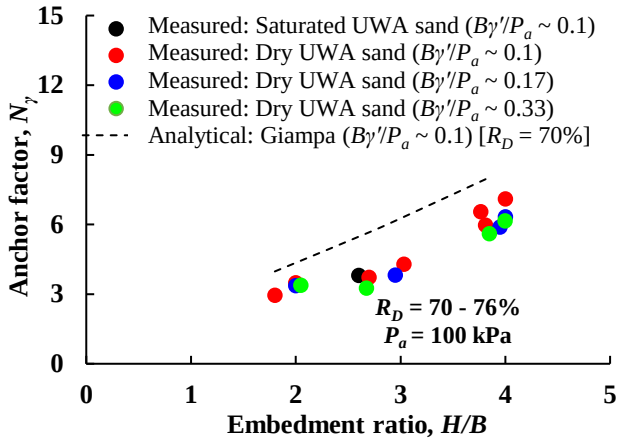

(a)

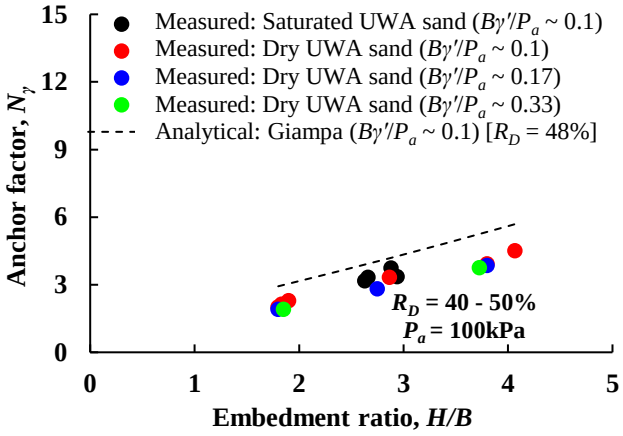

(b)

Fig. 6 : Comparison of measured N_γ for rectangular plates in dry and saturated drained conditions for (a) dense sand of R_D = 70% - 76% (b) medium dense sand of R_D = 40% - 50%

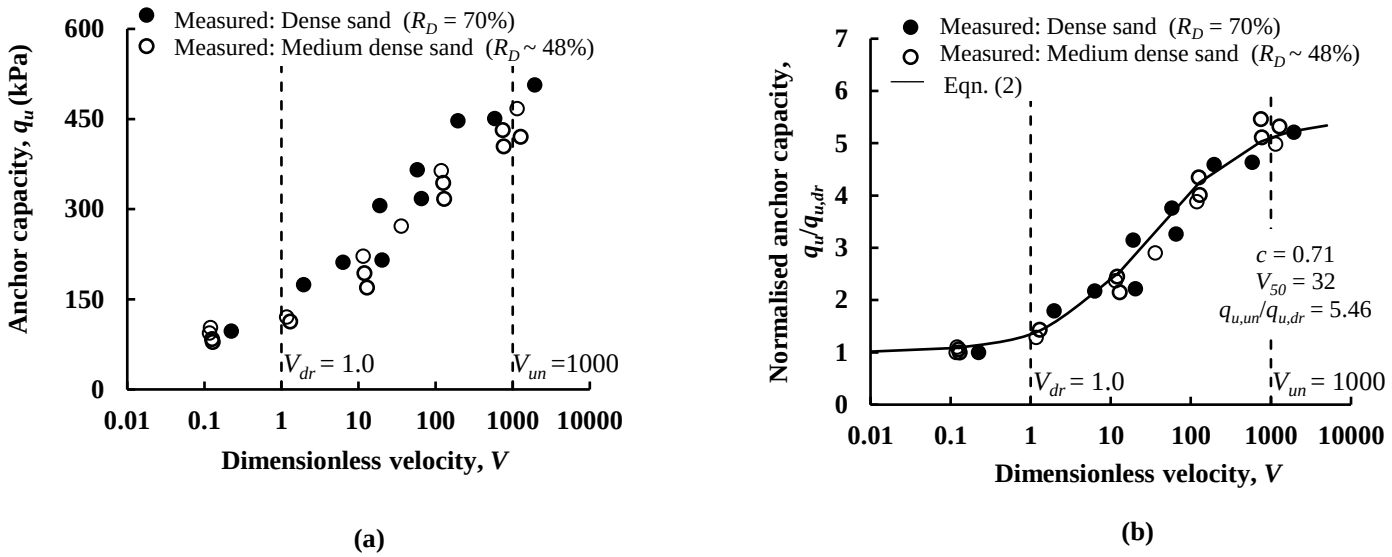

Fig. 7 : Changing anchor capacity with dimensionless velocity: (a) mobilised anchor capacity (q_u) and (b) normalised mobilised anchor capacity ($q_u/q_{u,dr}$)

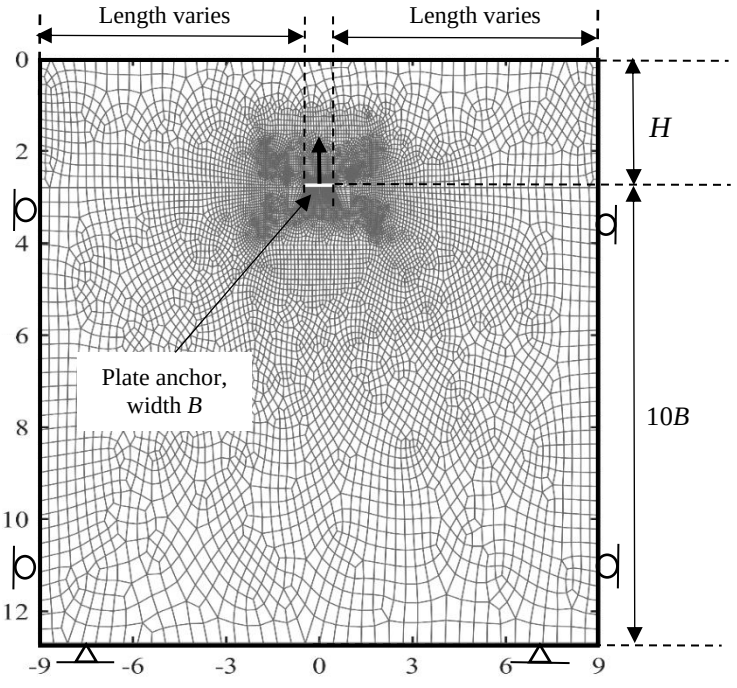

Fig. 8: Typical mesh details and boundary conditions for the anchor problem in Abaqus (H/B = 2.7)

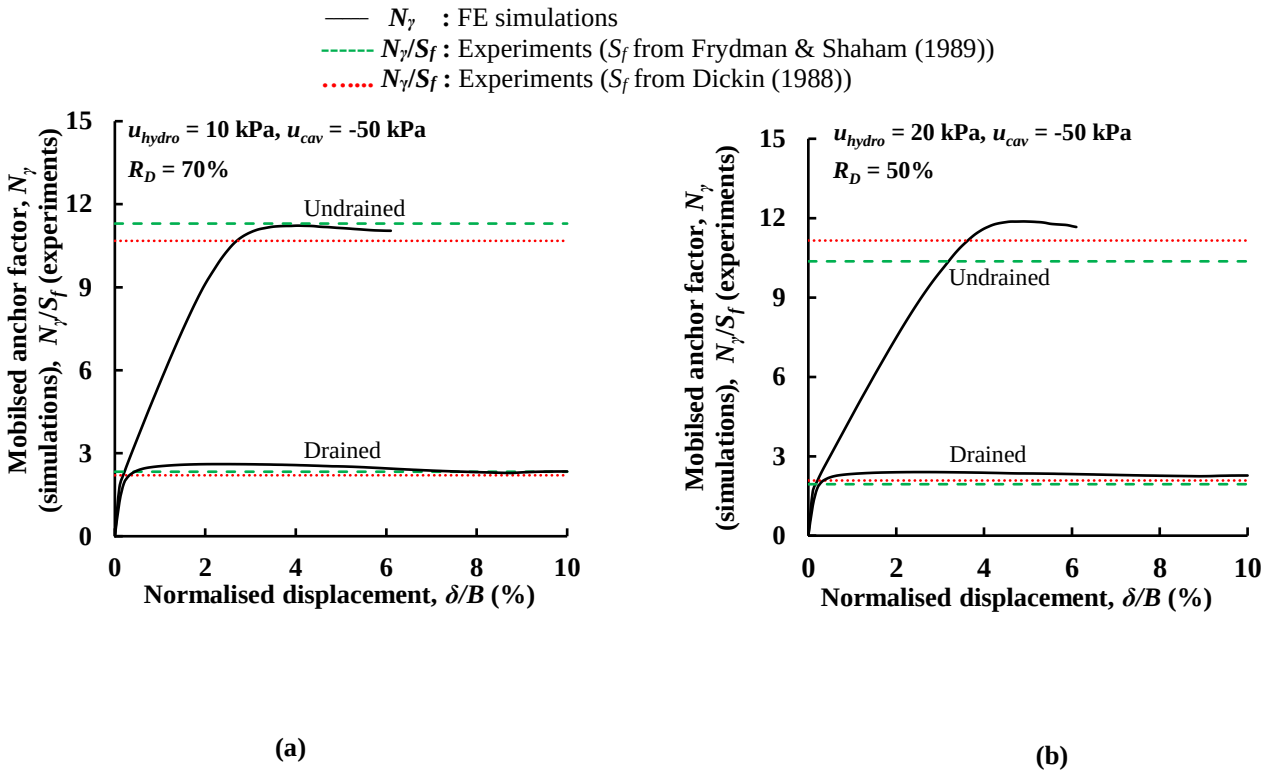

Fig. 9: Comparison of simulated and measured anchor factors (adjusted by shape factors) at H/B = 2.7 in: (a) dense sand (R_D = 70%) (b) medium dense sand (R_D = 50%)

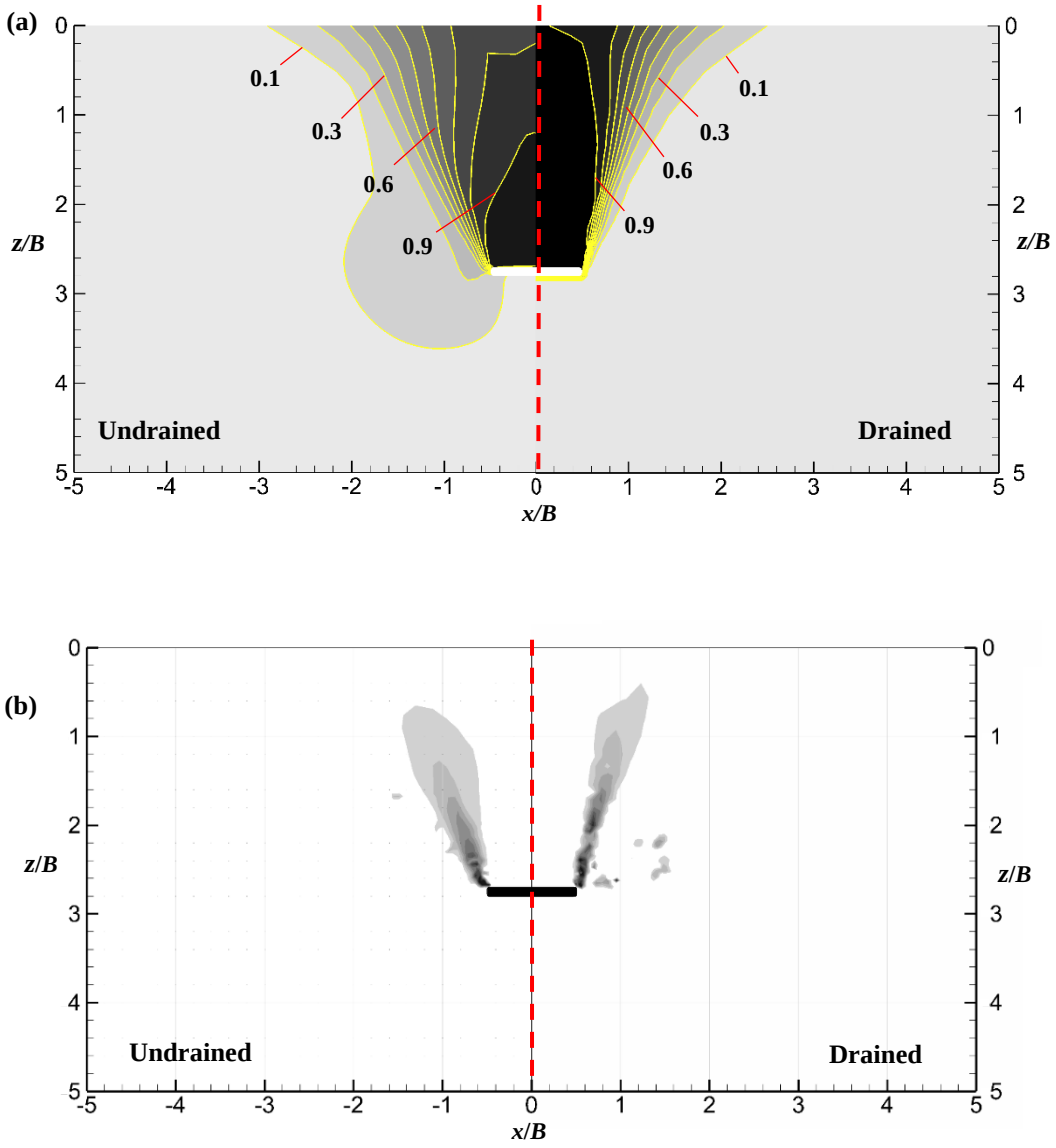

Fig. 10: Comparison of numerically determined: (a) failure mechanisms, (b) shear strain distributions at H/B = 2.7 in dense sand (R_D = 70%) for undrained and drained cases

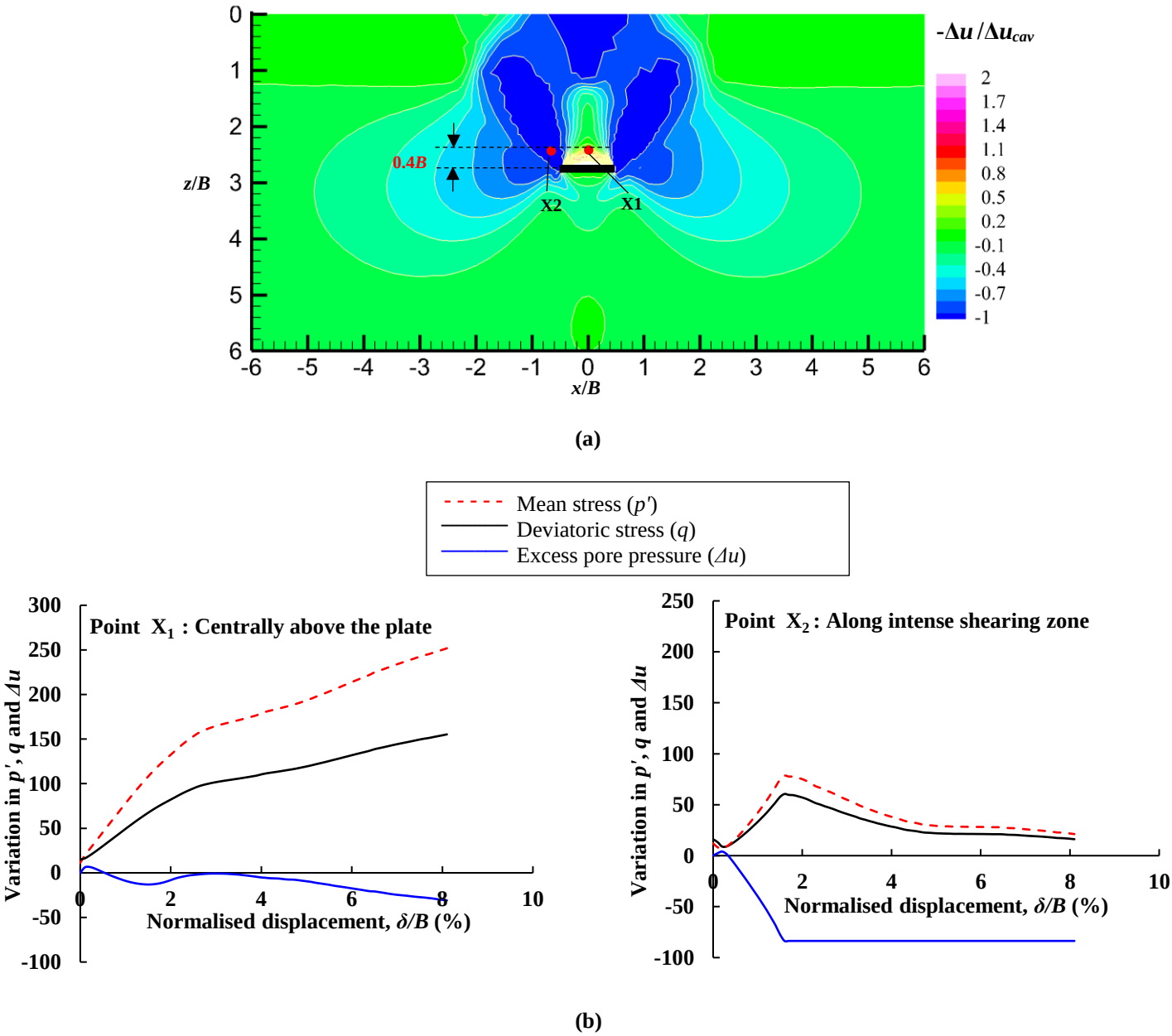

Fig. 11: (a) contours of excess pore pressure (Δu) normalised by the maximum possible pore pressure change possible prior to cavitation (Δu_{cav}) at H/B = 2.7 in R_D = 70% with u_{hydro} = 10 kPa (b) variation of p', q and Δu at two different points in the domain

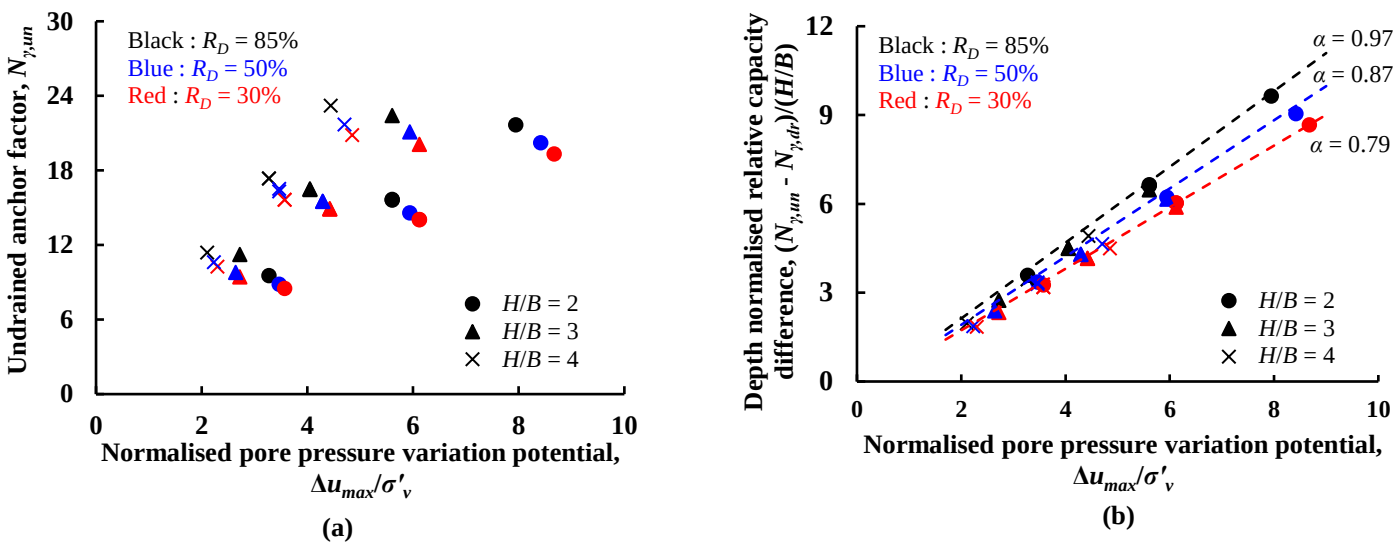

Fig. 12: Variation of: (a) $N_{\gamma,un}$ and (b) depth normalised relative difference, $\frac{N_{\gamma,un} - N_{\gamma,dr}}{H/B}$ from the FE simulations in dense and medium dense sands

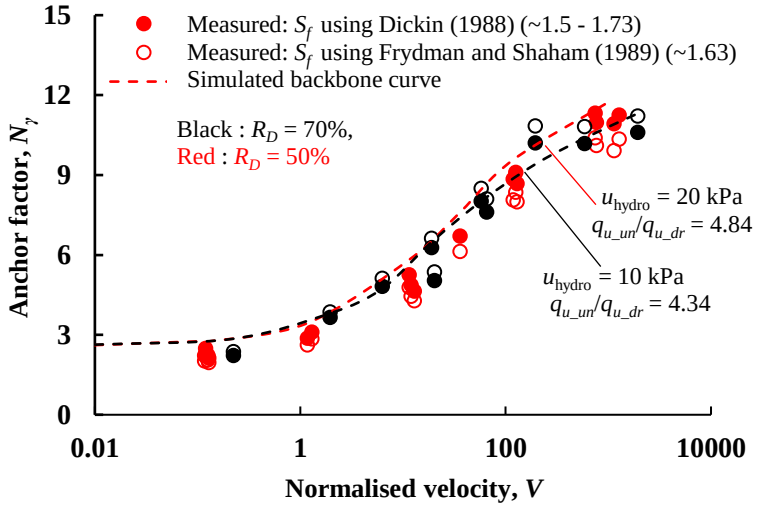

Fig. 13: Comparison of measured and predicted anchor factors with changing dimensionless velocity in dense and medium dense sand

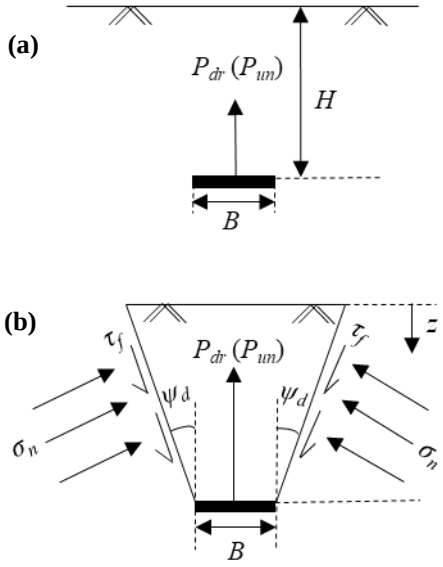

Fig. A1: Schematic representation of: (a) plate anchor uplift at failure (b) failure mechanism with inclined slip surface